International Journal of Creative and Open Research in Engineering and Management
ISSN: **3108-1754 (Online)**
Volume 02 Issue 06 June-2026 | Impact Factor: 3.5

Characterization of LED Emission Spectra Under Varying Thermal Conditions

Kakul[1], Mr. Vivek[2]
[1]Scholar, Faculty of Science, Shri Ram College, Muzaffarnagar
[2]Assistant professor, Shri Ram College, Muzaffarnagar
Correspondence Author Email: vivekroyal125@gmail.com,

How to Cite this Article:

Kakul, (2026). Characterization of LED Emission Spectra Under Varying Thermal Conditions. International Journal of Creative and Open Research in Engineering and Management, 02(6). https://doi.org/10.55041/ijcope.v2i6.234

License:

This article is published under the terms of the Creative Commons Attribution 4.0 International License (CC BY 4.0), which permits unrestricted use, distribution, and reproduction in any medium, provided the original author(s) and the source are credited.

© The Author(s). Published by International Journal of Creative and Open Research in Engineering and Management.

https://doi.org/ 10.55041/ijcope.v2i6.234

Abstract: This report investigates the electro-optical and thermodynamic mechanisms of light-emitting diodes (LEDs) under varying thermal conditions. It focuses on the impact of elevated junction temperatures (Tj) on LED emission spectra across different semiconductor materials, including Indium Gallium Nitride (InGaN) and Aluminum Gallium Indium Phosphide (AlGaInP). Utilizing a high-resolution optical spectrometer and a thermoelectric temperature control stage, the study finds that higher operating temperatures lead to a red shift in peak emission wavelengths and increased full-width at half-maximum, while reducing optical output power and internal quantum efficiency due to the activation of non-radiative recombination paths. Additionally, white LEDs experience significant thermal quenching effects, affecting color temperature and gamut. The study concludes with recommendations for high-efficiency micro-channel heat sinks and dual-junction measurement strategies to enhance reliability in optoelectronic systems.

I: INTRODUCTION

1.1 Introduction to Solid-State Lighting and LEDs: Over the past few decades, the global lighting paradigm has experienced a profound shift away from conventional incandescent and fluorescent systems toward Solid-State Lighting (SSL) frameworks driven by Light-Emitting Diodes (LEDs). This technological shift is largely a result of the fundamental physics governing electroluminescence in compound semiconductor materials. Unlike incandescent bulbs, which operate via thermal radiation (blackbody emission) requiring temperatures near 3000 K, or fluorescent tubes reliant on gas ionization and mercury excitation, LEDs convert electrical energy directly into narrow-band optical radiation through radiative recombination across a p-n junction active zone.

The advantages of this mechanism are profound: high electrical-to-optical conversion efficiencies, operational lifespans exceeding 50,000 hours, instantaneous modulation capabilities, and the exclusion of environmentally hazardous elements like mercury. Consequently, LEDs have transcended standard ambient lighting to become primary components across highly specialized fields, including:

- High-definition multi-micro-LED display panels.
- Solid-state automotive optical assemblies.
- Precision horticultural photostimulation matrix systems.
- Deep-tissue photodynamic medical equipment.

- Free-space optical communications (Li-Fi).

The advantages of LEDs over legacy light sources are substantial:

1. **High Luminous Efficacy:** Modern commercial LEDs regularly exceed 150 lm/W−200 lm/W, far outperforming incandescent bulbs (∼15 lm/W).
2. **Operational Lifespan:** LEDs offer rated operating lifetimes exceeding 50,000 hours, compared to a few thousand hours for traditional sources, significantly reducing replacement costs.
3. **Environmental Impact:** They eliminate hazardous materials like mercury, found in fluorescent tubes, while lowering carbon emissions through reduced energy consumption.
4. **Design Flexibility:** Their compact physical footprint and fast modulation capabilities enable precise control in applications ranging from micro-displays to automotive smart headlights.

1.2 The Role of Thermal Conditions in Optoelectronics: Despite these advantages, LEDs are not completely efficient. Current commercial sub-micron chips operate at electro-optical conversion efficiencies between 20% and 40%. The remaining 60% to 80% of input electrical energy is converted directly into heat via non-radiative recombination and ohmic losses across the internal resistance layers.

Because an LED chip typically has an active area smaller than 1 square mm, this heat generation creates high localized heat fluxes. If not effectively dissipated, the temperature at the microscopic p-n junction—known as the junction temperature (T_j)—can rapidly exceed 100◦C or even 150◦C.

In solid-state optoelectronics, the junction temperature is the primary factor limiting performance and long-term reliability. Elevated thermal states directly impact the semiconductor material's band structure, carrier distribution profiles, and structural stability. Consequently, understanding the relationship between thermal conditions and optical output is essential for engineering high-performance optoelectronic systems.

1.3 Problem Statement: When an LED operates under real-world conditions, its emission spectrum does not remain static. As the junction temperature rises due to ambient changes or internal self-heating, the emission spectrum undergoes distinct modifications:

- The peak emission wavelength shifts toward longer wavelengths (red shift) or, in unique multi-quantum well structures, exhibits complex non-linear drifts.
- The spectral line-shape broadens, degrading color purity in narrow-band displays.
- The total optical power decreases through thermal quenching, causing a drop in luminous flux.

In multi-die or phosphor-converted white LED systems, these changes cause a significant shift in chromaticity coordinates, an unpredictable drift in Correlated Color Temperature (CCT), and a decline in the Color Rendering Index (CRI).

For applications requiring precise emission characteristics—such as high-density optical data storage, visible light communication (Li-Fi), medical phototherapy, and outdoor automotive signaling—these thermally driven spectral changes can lead to system failures. There is a clear need for precise models and experimental data that characterize how LED emission spectra behave under varying thermal conditions.

1.4 Research Objectives: This university project report systematically investigates and quantifies the changes in LED emission spectra across a wide thermal range. The primary objectives are:

- To establish the theoretical framework governing carrier dynamics, bandgap variations, and radiative/non-radiative recombination balances as a function of temperature.
- To design and assemble an automated experimental apparatus capable of isolating and controlling the ambient thermal environment of an LED while measuring its real-time spectral output.
- To characterize the temperature-dependent variations in peak wavelength (λ_p), full-width at half-maximum ($\Delta\lambda_{FWHM}$), and integrated optical power across different semiconductor materials (InGaN, AlGaInP, and phosphor-converted white LEDs).
- To extract underlying physical material coefficients, such as the Varshni parameters (α, β), using experimental spectral data.
- To evaluate thermal management techniques and measurement protocols to minimize heat-induced spectral degradation in real-world engineering applications.

1.5 Scope and Organization of the Report: The scope of this study is bounded by steady-state thermal conditions ranging from 283 K to 363 K (10°C to 90°C), representing standard commercial and automotive operating environments. The electrical excitation is primarily focused on constant-current continuous-wave (CW) modes, though pulsed current techniques are evaluated to differentiate between internal self-heating and ambient thermal variations. The report is organized into the following chapters:

- Part 2 reviews the underlying physics of semiconductor luminescence, focusing on energy band structures, recombination mechanisms, and the theoretical models for temperature-induced bandgap narrowing and spectral broadening.
- Part 3 outlines the experimental methodology, detailing the instrumentation, optical alignment, calibration procedures, and methods used to extract the junction temperature.
- Part 4 presents the experimental results and discussion, focusing on the characterization of monochromatic and phosphor-converted white LEDs.
- Part 5 discusses practical engineering applications, including thermal management configurations, optical compensation strategies, and advanced testing protocols.
- Part 6 summarizes the findings, outlines the main contributions, and proposes areas for future research.

II: THEORETICAL FRAMEWORK & SEMICONDUCTOR PHYSICS

2.1 Physics of Semiconductor Luminescence: The conversion of electrical energy into optical radiation within a Light-Emitting Diode (LED) is governed by the principles of quantum mechanics and solid-state physics. This process, known as injection electroluminescence, occurs when a semiconductor p-n junction is subjected to an external forward bias. To understand the micro-mechanisms that dictate the shape, intensity, and temperature sensitivity of the resulting emission spectrum, we must examine the underlying electronic band structures, carrier injection dynamics, and quantum conservation laws.

2.1.1 Energy Band Structures and the Direct Band gap Prerequisite: In a crystalline solid, the periodic potential of the atomic lattice splits the available electronic energy states into distinct allowed bands separated by forbidden energy gaps. The two bands critical to optoelectronic operation are:

1. **The Valence Band (V_B):** The highest range of electron energies in which electrons are normally present at absolute zero temperature.
2. **The Conduction Band (C_B):** The lowest range of vacant electronic states into which electrons can be thermally or electrically excited, gaining mobility to conduct electrical current.

The energy differential between the floor of the conduction band (E_c) and the roof of the valence band (E_v) defines the fundamental bandgap energy (E_g):

$$E_g = E_c - E_v$$

For an electron in the conduction band to drop into an empty state (hole) in the valence band and emit a photon, the transition must satisfy the fundamental conservation laws of physics: Conservation of Energy and Conservation of Momentum.

The momentum ($\mathbf{p}$) of a charge carrier in a crystal lattice is related to its wave vector ($\mathbf{k}$) via the de Broglie relation:

$$\mathbf{p} = \hbar\mathbf{k}$$

Where $\hbar$ is the reduced Planck constant ($h/2\pi$). Therefore, electronic transitions are analyzed within the energy-momentum (E- $\mathbf{k}$) space.

Semiconductor materials are categorized into two structural classes based on their (E- $\mathbf{k}$) profiles:

I. Direct-Bandgap Semiconductors: In direct-bandgap materials—such as Gallium Nitride (GaN), Indium Gallium Nitride (InGaN), and Aluminum Gallium Indium Phosphide (AlGaInP)—the minimum of the conduction band and the maximum of the valence band align perfectly at the same crystal momentum vector, typically at the center of the first Brillouin zone ($\mathbf{k} = 0$, known as the Γ-point).

$$\mathbf{k}_c = \mathbf{k}_v = 0$$

When an electron at the conduction band edge recombines with a hole at the valence band edge, the change in momentum $\Delta\mathbf{k}$ is zero. A photon carries a negligible wavevector ($\mathbf{k}_{photon} = 2\pi / \lambda \approx 0$ relative to the scale of the crystal Brillouin zone). Consequently, the transition satisfies momentum conservation directly:

$\mathbf{k}_c - \mathbf{k}_v = \mathbf{k}_{photon} \approx 0$

Because no secondary momentum-matching particles are required, the probability of a radiative transition is high. The carrier lifetime for radiative recombination in direct materials is short (typically on the order of nanoseconds), making them highly efficient optical emitters.

II. Indirect-Bandgap Semiconductors: In indirect-bandgap materials—such as Silicon, Germanium and Gallium Phosphide (GaP), the conduction band minimum is shifted to a non-zero wave vector ($\mathbf{k}_c \neq 0$), while the valence band maximum remains at the Γ-point ($\mathbf{k}_v = 0$).

An electron at the bottom of the conduction band cannot drop directly into a valence band hole because the momentum discrepancy ($\Delta\mathbf{k} = \mathbf{k}_c - \mathbf{k}_v \neq 0$) cannot be absorbed by the emitted photon alone. To conserve momentum, the transition must involve a third body: a quantized lattice vibration known as a phonon. This process can occur via two pathways:

- **Phonon Emission:** The electron releases excess momentum as a lattice vibration while simultaneously emitting a photon.
- **Phonon Absorption:** The electron absorbs a lattice phonon to match momentum coordinates before dropping across the bandgap.

Because this represents a second-order quantum mechanical process requiring the simultaneous interaction of three entities (electron, hole, and phonon), its probability is orders of magnitude lower than direct recombination. Instead of generating light, the excess energy is typically dissipated as heat through non-radiative pathways. Therefore, efficient LED design requires direct-bandgap alloy systems.

2.1.2 Carrier Injection and Non-Equilibrium Dynamics: An LED under zero thermal and electrical bias rests in thermodynamic equilibrium. The Fermi energy level (E_F) is uniform throughout the p-n junction, creating a built-in electrostatic potential barrier (V_{bi}) across the depletion region that prevents majority carriers (electrons in the n-type layer, holes in the p-type layer) from diffusing across the junction.

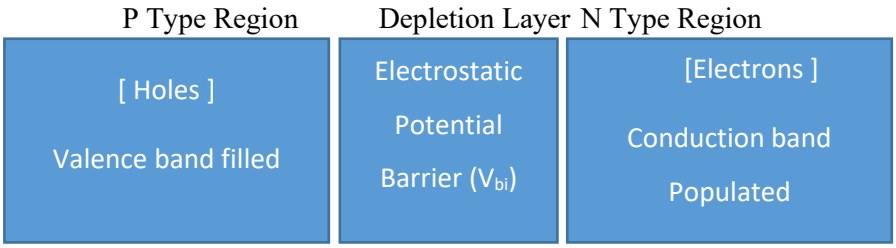

Figure 1: Thermodynamic Equilibrium in LED

When an external forward bias voltage (V_F) is applied to the device, it opposes and reduces the built-in potential barrier. The depletion width narrows, and the flat Fermi level splits into two distinct Quasi-Fermi levels: E_{Fc} for electrons in the conduction band and E_{Fv} for holes in the valence band. The separation between these quasi-Fermi levels corresponds directly to the applied electrical work:

$E_{Fc} - E_{Fv} = qV_F$

Where q is the elementary elementary electron charge. This reduction in the potential barrier enables massive carrier injection:

1. Electrons from the n-side are injected across the depletion zone into the p-side (or into an undoped multi-quantum well active layer).
2. Holes from the p-side are simultaneously injected into the same active zone.

This injection creates a localized, high-density population of excess, non-equilibrium minority carriers within the active layer. The system seeks to restore thermodynamic equilibrium by eliminating these excess electron-hole pairs through recombination.

2.1.3 Microscopic Recombination Kinetics: Once injected, electrons and holes scatter elastically via carrier-carrier and carrier-phonon collisions. This process occurs on a sub-picosecond timescale, causing the carriers to lose excess kinetic energy and settle ("thermalize") near the absolute edges of their respective bands (E_c and E_v). From these thermalized positions, the final radiative transition occurs. The rate of spontaneous radiative recombination (R_{sp}) per unit volume per unit energy interval is determined by the transition matrix element derived from Fermi's Golden Rule:

$$R_{sp}(E) = \frac{4q^2 n_r E}{m_0^2 c^3 \hbar^2} |M_b|^2 \, . \, N_J(E) \, . \, f_c(E_c) \, f_v(E_v)$$

Where n_r is the refractive index of the semiconductor medium, m_0 is the free electron mass, $|M_b|^2$ is the momentum matrix element for the interband transition, which quantifies the quantum mechanical overlap between the electron and hole wavefunctions, $N_J(E)$ is the joint density of states, defining the number of pairs of conduction and valence states per unit volume per unit energy separated by an energy E & $f_c(E_c)$ and $f_v(E_v)$ are the Fermi-Dirac occupation probabilities for the conduction and valence band edges, respectively.

Under high forward injection currents, the total radiative recombination rate is typically modeled as a bimolecular process proportional to the product of the free electron density (n) and free hole density (p):

$$R_{radiative} = B \, . \, n \, . \, p$$

Where B is the bimolecular radiative recombination coefficient. Because B depends on the thermal velocity of the carriers and the localized alignment of wavefunctions in k-space, it exhibits a strong temperature dependence ($B \propto T^{-3/2}$). This decay profile represents a primary physical mechanism driving thermal quenching at elevated junction temperatures.

2.1.4 Spectral Line-Shape Origins: The theoretical shape of the emitted spontaneous spectrum is not an infinitely sharp delta function at the bandgap energy E_g, but rather a broadened distribution. This profile is determined by the combined mathematical properties of the joint density of states and the carrier distribution functions.

For a three-dimensional bulk semiconductor crystal, the joint density of states scales as a square-root function of the energy excess above the bandgap:

$$N_J(E) \propto \sqrt{(E - E_g)} \text{ for } E \geq E_g$$

This square-root dependence creates a sharp cut-off on the long-wavelength (low-energy) side of the emission spectrum because no electronic states exist within the forbidden band gap ($E < E_g$).

Conversely, the population profile of carriers extending upward into the higher-energy states of the conduction and valence bands is governed by Fermi-Dirac distribution functions. For non-degenerate injection levels, these distributions can be closely approximated using classical Maxwell-Boltzmann statistics:

$$f_c(E_c) \, f_v(E_v) \propto \exp -\frac{E - E_g}{k_B T}$$

Where k_B is the Boltzmann constant and T is the absolute junction temperature (T_j). The spectral intensity distribution, I(E), is proportional to the product of these two opposing functions:

$$I(E) \propto \sqrt{(E - E_g)} \, . \exp \{-\frac{E - E_g}{k_B T}\}$$

This product creates the characteristic asymmetric line shape of monochromatic LED emissions:

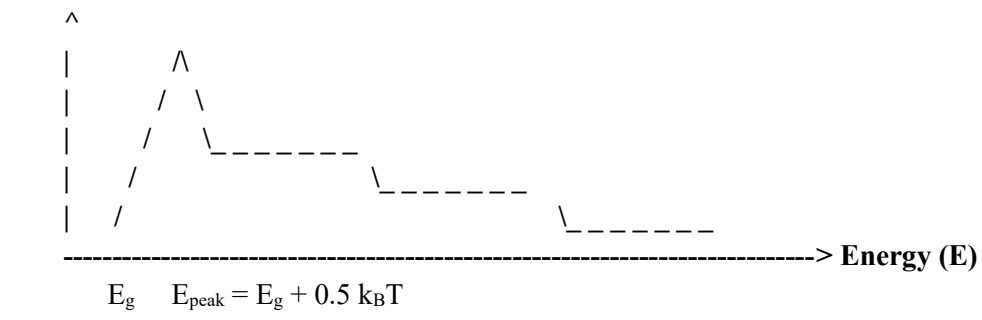

Figure 2 : Spontaneous Emission Spectrum Profile

1. **The Low-Energy Base:** At $E = E_g$, the intensity starts from zero, driven by the $\sqrt{(E - E_g)}$ term. It rises sharply as more electronic states become available.
2. **The Peak Position:** The maximum of the curve is found by differentiating I(E) with respect to E and setting it to zero:

$$\frac{dI(E)}{dE} = 0 \Longrightarrow E_{peak} = E_g + \frac{1}{2} k_B T$$

This shows that the highest emission intensity occurs slightly above the fundamental bandgap energy due to the thermal kinetic energy of the carrier distribution.

3. **The High-Energy Tail:** Beyond the peak, the exponential term $\exp\frac{-(E-E_g)}{k_B T}$ dominates. The intensity decreases as energy increases, creating an extended tail on the short-wavelength side.

As the junction temperature (T_j) varies, both the position of E_g (via Varshni' s narrowing effects) and the slope of the high-energy tail change. This dual dependence alters the peak emission wavelength and broadens the spectral linewidth.

2.2 Energy Band Structure and Bandgap Temperature Dependence: The fundamental bandgap energy (E_g) of semiconductor crystals is not constant; it decreases as temperature increases. This bandgap narrowing is driven by two primary physical mechanisms:

1. **Thermal Expansion of the Crystal Lattice:** As temperature rises, increased lattice vibrations increase the average interatomic spacing. This change alters the periodic potential experienced by the valence electrons, generally reducing the bonding strength and lowering the energy separation between the bonding valence states and antibonding conduction states.
2. **Electron-Phonon Interactions:** Quantum mechanical scattering between charge carriers and lattice vibrations (phonons) shifts the self-energy levels of both the electrons and holes, modifying the effective band edge positions.

To model this temperature dependence, Varshni proposed a widely accepted semi-empirical equation:

$$E_g(T) = E_g(0) - \frac{\alpha T^2}{T+\beta}$$

Where $E_g(0)$ is the material's bandgap energy extrapolated to absolute zero (0 K), α (eV/K) is an empirical parameter reflecting the strength of the electron-phonon interaction, β (K) is a material constant closely related to the Debye temperature of the crystal lattice.

An alternative formulation based on Bose-Einstein phonon distribution models, proposed by O' Donnell and Chen, provides additional physical insight into high-temperature regimes:

$$E_g(T) = E_g(0) - S\langle h\nu\rangle \coth\left(\frac{\langle h\nu\rangle}{2k_B T}\right) - 1$$

Where S is a dimensionless coupling constant and $\langle h\nu\rangle$ represents the average phonon energy. Both models show that as the junction temperature rises, the fundamental emission threshold shifts toward lower energies, causing a red shift in the peak wavelength:

$$\lambda_p(T) \approx \frac{hc}{E_g(T)}$$

2.3 Carrier Distribution and Joint Density of States: To precisely model the shape, asymmetric width, and thermal evolution of an LED's emission spectrum, we must mathematically evaluate how electronic states are distributed within the semiconductor bands and how injected carriers occupy those states. This requires analyzing the quantum mechanical derivation of the Joint Density of States (JDOS) alongside the statistical thermodynamics governing carrier distribution profiles.

2.3.1 Derivation of Density of States in Dimensional Systems: The Density of States (DOS), denoted as N(E), defines the number of available quantum states per unit volume per unit energy interval. Its mathematical formulation depends heavily on the spatial dimensionality and confinement geometry of the active region.

I. Bulk Three-Dimensional (3D) Semiconductors: In a bulk semiconductor layer where carriers move freely in all three spatial dimensions, we solve the time-independent Schrödinger equation using periodic boundary conditions within a cube of side length L. The permitted wavevector states in k-space form a cubic grid:

$k_x = \frac{2\pi n_x}{L}$, $k_x = \frac{2\pi n_x}{L}$, $k_x = \frac{2\pi n_x}{L}$, $(n_x, n_y, n_z \in Z)$

The volume of a single state in k-space is $(2\pi/L)^3$. The total number of states N_k within a spherical shell of radius k is given by dividing the spherical volume by the single-state volume, multiplying by 2 to account for electron spin degeneracy:

$$N_k = 2 \cdot \frac{\frac{4}{3}\pi k^3}{\left(\frac{2\pi}{L}\right)^3} = \frac{V}{3\pi^2}k^3$$

Where $V = L^3$ is the crystal volume. Assuming a parabolic band approximation near the zone center Γ-point), the kinetic energy E of an electron in the conduction band is related to its wavevector by:

$E = E_c + \frac{\hbar^2 K^2}{2m_c^*}$

Substituting $k = \frac{2m_c^*}{\hbar^2 K^2}(E - E_c)^{1/2}$ into the state equation and differentiating with respect to energy (dN_k/dE) yields the conduction band density of states per unit volume:

$$N_c(E) = \frac{1}{2\pi^2}\left(\frac{2m_c^*}{\hbar^2}\right)^{3/2}\sqrt{E - E_c} \quad (E \geq E_c)$$

Similarly, for holes near the valence band edge:

$$N_v(E) = \frac{1}{2\pi^2}\left(\frac{2m_v^*}{\hbar^2}\right)^{3/2}\sqrt{E_v - E} \quad (E \leq E_v)$$

II. Two-Dimensional (2D) Quantum Wells: When the active layer thickness is reduced to the nanometer scale (less than the de Broglie wavelength of the carriers), motion along the growth axis (z-axis) becomes quantized into discrete energy levels (E_n), while carriers remain free to move in the xy-plane.

The k-space domain collapses into two-dimensional circles. The area of a single state is $(2\pi/L)^2$. Following a similar derivation using area parameters, the density of states becomes independent of continuous energy variations between steps, forming a staircase profile:

$N_{2D}(E) = \frac{m^*}{\pi\hbar^2}\,\Theta(E - E_n)$

Where Θ is the Heaviside step function. This step-like profile concentrates carrier densities at lower energy states, enhancing the radiative recombination probability in multi-quantum well (MQW) configurations.

2.3.2 The Concept of Joint Density of States (JDOS): Optical emission does not depend on isolated individual band densities, but on the simultaneous availability of an occupied electron state in the conduction band and an empty hole state in the valence band that share identical momentum vectors ($k_c = k_v$). This requirement makes the Joint Density of States $\mathbf{N_J(E)}$ the primary factor shaping the emission spectrum.

For an optical transition with photon energy $h\upsilon = E$, the energy separation between the two states is:

$E = E_c(\mathbf{k}) - E_v(\mathbf{k}) = E_g + \frac{\hbar^2 k^2}{2m_c^*} + \frac{\hbar^2 k^2}{2m_v^*} = E_g + \frac{\hbar^2 k^2}{2m_r^*}$

Where m_r^* is the reduced effective mass of the electron-hole system, defined by:

$\frac{1}{m_r^*} = \frac{1}{m_c^*} + \frac{1}{m_v^*}$

By using m_r^* to represent the system's effective mass, the individual band equations can be combined. For a 3D bulk semiconductor, this yields the complete expression for the Joint Density of States:

$N_J(E) = \left(\frac{1}{2\pi^2}\frac{2m_r^*}{\hbar^2}\right)^{3/2}\sqrt{(E - E_g)} \quad (E \geq E_g)$

This square-root dependence sets the hard physical boundary for the long-wavelength edge of the LED spectrum: at photon energies below the bandgap ($E < Eg$), $N_J(E) = 0$, meaning no optical transitions can occur.

2.3.3 Statistical Thermodynamics of Carrier Distribution: While the JDOS determines the available transitions, the actual emission profile depends on how injected carriers are distributed across these states. This distribution is governed by quantum statistical mechanics.

I. Fermi-Dirac Distribution: Electrons and holes are fermions (s = 1/2) and obey the Pauli's exclusion principle. Their steady-state occupancy probabilities are defined by the Fermi-Dirac distribution functions:

$f_c(E) = \frac{1}{1 + exp\ \frac{E - E_{Fc}}{k_B T}}$, $f_v(E) = \frac{1}{1 + exp\ \frac{E - E_{Fv}}{k_B T}}$,

Where E_{Fc} and E_{Fv} are the non-equilibrium electron and hole Quasi-Fermi levels established by the forward bias.

II. Maxwell-Boltzmann Approximation: In typical high-brightness LED applications operating at standard current densities, the injected carrier concentration remains low enough that the Quasi-Fermi levels reside within the forbidden bandgap, at least several k_BT away from the band edges ($E_c - E_{Fc} >> k_BT$). Under these non-degenerate conditions, the exponential term in the denominator becomes much larger than 1, allowing the Fermi-Dirac distribution to simplify to the classical Maxwell-Boltzmann distribution:

$f_c(E) \approx \exp - \frac{E - E_{Fc}}{k_B T}$

This approximation shows that the probability of finding a carrier at a higher energy state decreases exponentially with energy, scaled by the available thermal energy (k_BT).

2.3.4 Mathematical Synthesis of the Spontaneous Spectrum: The spontaneous emission spectral intensity I(E) as a function of energy is proportional to the product of the structural joint density of states and the statistical carrier distribution profiles:

$I(E) \propto N_J(E) .\ f_c(E_c) .\ [1 - f_v(E_v)]$

Using the Maxwell-Boltzmann approximation, this simplifies to:

$I(E) = C .\ \sqrt{(E - Eg)} .\ \exp \frac{-(E - Eg)}{k_B T}$ (E≥Eg)

Where C is a temperature-dependent proportionality constant that accounts for structural matrix elements and refractive indices.

I. Extraction of the Analytical Emission Peak (E_{peak}): To find the energy where maximum emission intensity occurs, we differentiate I(E) with respect to energy E and solve for zero:

$\frac{dI(E)}{dE} = C \frac{1}{2\sqrt{(E - Eg)}} \exp \frac{-(E - Eg)}{k_B T} - \frac{\sqrt{(E - Eg)}}{k_B T} \exp \frac{-(E - Eg)}{k_B T} = 0$

Dividing both sides by the exponential term and restructuring gives:

$\frac{1}{2\sqrt{(E - Eg)}} = \frac{\sqrt{(E - Eg)}}{k_B T} \implies E - Eg = \frac{1}{2} k_B T$

$E_{peak}(T) = E_g(T) + \frac{1}{2} k_B T$

This result shows that as temperature increases, the peak of the 1emission spectrum experiences competing shifts: it moves toward lower energies due to the narrowing of the fundamental bandgap $E_g(T)$, but is pulled toward higher energies by the expanding thermal energy term (+0.5 k_BT). Since bandgap narrowing typically dominates, the net result is a red shift.

II. Analytical Derivation of the Full-Width at Half-Maximum (ΔE_{FWHM}): The Full-Width at Half-Maximum is defined as the energy interval ($\Delta E = E_2 - E_1$) where the spectral intensity drops to exactly half of its peak value:

$I(E_{1,2}) = \frac{1}{2} I(E_{peak})$

Substituting $E_{peak} - E_g = 0.5\ k_BT$ into the core intensity equation gives the half-maximum condition:

$\sqrt{(E - Eg)} .\ \exp \frac{-(E - Eg)}{k_B T} = \frac{1}{2} \sqrt{(\frac{k_B T}{2})} .\ \exp \frac{-1}{2}$

We define a normalized dimensionless energy variable x = E - Eg{kB T. The half-maximum expression then simplifies to:

$\sqrt{x} .\ e^{-x} = \frac{1}{2\sqrt{(2e}}$ = approx 0.2131

Squaring both sides yields a transcendental equation:

$x .\ e^{-2x} = \frac{1}{8e}$ = approx 0.04598

This equation has two real roots, which can be solved numerically using Lambert W functions:

- Lower half-power point (x_1): x_1 (approx 0.086)

- Upper half-power point ($\mathbf{x_2}$): x_2 (approx 1.842)

Converting these roots back to energy units:

$E_1 = E_g + 0.086\ k_BT$

$E_2 = E_g + 1.842\ k_BT$

The theoretical energy linewidth ΔE_{FWHM} is the difference between these two values:

$\Delta E_{FWHM} = E_2 - E_1 = (1.842 - 0.086)\ k_BT \approx 1.756\ k_BT \approx 1.8\ k_BT$

This linear dependence on k_BT explains why the emission spectra of monochromatic LEDs broaden systematically at elevated junction temperatures. Higher temperatures expand the thermal distribution of carriers, populating high-energy states and broadening the high-energy tail of the spectrum.

2.4 Radiative vs. Non-Radiative Recombination Mechanisms: The total current injected into an LED (I_F) splits into radiative and non-radiative components. This balance is commonly modeled using the standard ABC recombination framework:

$I_{total} = qV_{active}\ AN + BN^2 + CN^3 + I_{leak}$

Where N is the carrier density within the active volume (V_{active}), A(s^{-1}) is the Shockley-Read-Hall (SRH) non-radiative recombination coefficient, representing carrier trapping by crystal defects and deep-level impurities, B (cm^3/s) is the bimolecular radiative recombination coefficient, C (cm^6/s) is the non-radiative Auger recombination coefficient, where excess energy is transferred to a third carrier rather than creating a photon and I_{leak} represents carrier leakage out of the active confinement zone.

Each coefficient exhibits distinct temperature dependencies that degrade efficiency at higher temperatures:

- The radiative coefficient (T) decreases with temperature ($\propto T^{-3/2}$ for bulk materials) because carrier thermal velocity spreads out wavefunction overlap in **k**-space.
- The SRH coefficient A(T) typically increases at higher thermal states as carrier capture cross-sections expand due to multi-phonon assistance.
- Thermal activation allows carriers to overcome the heterostructure barrier heights (e.g., AlGaN barriers in InGaN quantum wells), increasing I_{leak}.

The Internal Quantum Efficiency (IQE), defined as the ratio of radiative recombination to total recombination, drops significantly as temperature rises:

$$IQE(T) = \frac{BN^2}{AN + BN^2 + CN^3}$$

This reduction in IQE is known as thermal quenching.

2.5 Multi-Quantum Well (MQW) Effects and Carrier Localization: The transition from bulk semiconductor homojunctions to heterostructure designs featuring nanometer-scale Multi-Quantum Wells (MQWs) represents a major milestone in high-brightness LED engineering. While MQW structures significantly improve radiative efficiency at room temperature, their optical properties exhibit complex variations when subjected to fluctuating thermal environments.

To analyze these characteristics, we must evaluate the quantum confinement mechanisms, the role of localized alloy fluctuations, the structural impact of internal electric fields, and the thermal carrier dynamics that dictate spectral emission pathways.

2.5.1 Quantum Confinement and Modified Density of States: In an MQW architecture, thin layers of a lower-bandgap semiconductor (the wells, such as $In_xGa_{1-x}N$) are sandwiched between layers of a wider-bandgap material (the barriers, such as GaN). When the well thickness (L_z) approaches the de Broglie wavelength of the injected carriers (typically 2 nm - 5 nm), quantum confinement effects restrict carrier motion along the growth axis (z-axis).

This spatial restriction forces the continuous bulk conduction and valence bands to split into discrete, quantized energy subbands (E_n for electrons, H_m for holes). The bound state energy levels within an infinitely deep quantum well are defined by:

$$E_n = \frac{\hbar^2}{2m^*}\ \frac{n\pi^2}{L_z} \quad (n = 1, 2, 3, ,,,,,,,)$$

This quantum confinement modifies the Joint Density of States (JDOS). The bulk square-root dependence ($\sqrt{(E-E_g)}$) is replaced by a step-like mathematical function:

$N_{J,2D}(E) = \frac{mr^*}{\pi \hbar \hat{} 2\, Lz} n\theta(E - E_n)$

Where θ is the Heaviside step function and E_n is the transition energy between the n-th electron and hole subbands.

This staircase profile provides a key operational advantage: it creates a high density of states right at the lowest allowable transition energy (E_1). Injected carriers quickly thermalize to this step edge rather than spreading thin across a broad energy range, matching electron and hole positions to maximize the radiative recombination rate ($R_{radiative} \propto Bnp$).

2.5.2 Nanoscale Alloy Fluctuations and Localization Energy Potential

In ternary and quaternary alloy systems—specifically Indium Gallium Nitride ($In_xGa_{1-x}N$) used for blue/green emission and Aluminum Gallium Indium Phosphide (AlGaInP) used for red/amber emission—the structural lattice is prone to local atomic variations. Because Indium atoms have a larger ionic radius than Gallium atoms, they tend to cluster during epitaxial crystal growth, creating random fluctuations in the local alloy composition. These local variations in Indium concentration alter the semiconductor bandgap on a nanometer scale:

- Regions with higher Indium concentrations exhibit a locally lower bandgap.
- Regions with lower Indium concentrations maintain a higher bandgap.

These lower-bandgap clusters create localized potential energy wells (potential minima) embedded within the broader 2D quantum well layer. The depth of these potential wells defines the localization energy (E_{loc}), which typically ranges from 10 MeV to over 50 MeV depending on the average Indium fraction.

These localization sites act as protective quantum traps for charge carriers. At low temperatures, injected electrons and holes fall into these local minima. Once trapped, they are physically isolated from non-radiative defects, such as threading dislocations, that propagate through the GaN template.

This carrier localization mechanism enables InGaN-based LEDs to maintain high internal quantum efficiency despite containing high defect densities (10^8 - 10^9 cm^{-2}).

2.5.3 The Quantum-Confined Stark Effect (QCSE) and Piezoelectric Fields: Most commercial nitride-based LEDs are grown along the polar c-axis ([0001] direction) of the wurtzite crystal structure. This orientation introduces a major physical challenge: strong internal electric fields (F_{int}) within the active multi-quantum wells. These fields arise from two distinct sources:

1. **Spontaneous Polarization:** Built-in polarization caused by the non-centrosymmetric atomic structure of the wurtzite lattice.
2. **Piezoelectric Polarization:** Strain-induced polarization resulting from the significant lattice mismatch between the thin InGaN well layers and the surrounding GaN barrier matrices.

The combined internal electric field can exceed 1 MV/cm. This field tilts the potential energy profile of the quantum wells, causing a spatial separation of the carrier wavefunctions known as the Quantum-Confined Stark Effect (QCSE).

The QCSE modifies the emission spectrum through two primary mechanisms:

1. **Spatial Decoupling:** The internal field pushes electrons toward one side of the quantum well and holes toward the opposite side. This reduces the spatial overlap integral ($\langle\psi_e|\psi_h\rangle$) between their quantum wavefunctions, lowering the radiative transition probability and increasing the carrier lifetime.
2. **Electrostatic Band-Bending:** The tilted potential energy profile narrows the effective energy separation between the lowest electron subband and the highest hole subband, shifting the primary emission peak to an energy lower than the material's bulk bandgap ($E_{emission} < E_g$).

2.5.4 Thermal Carrier Dynamics and the "S-Shaped" Spectral Trend: As the junction temperature (T_j) increases from cryogenic levels to high operating temperatures, the interaction between carrier localization and the QCSE produces a non-linear, "S-shaped" shift in the peak emission wavelength λ_p or E_{peak}. This behavior deviates significantly from the standard monotonic red shift predicted by Varshni's empirical equation.

Peak Energy Epeak

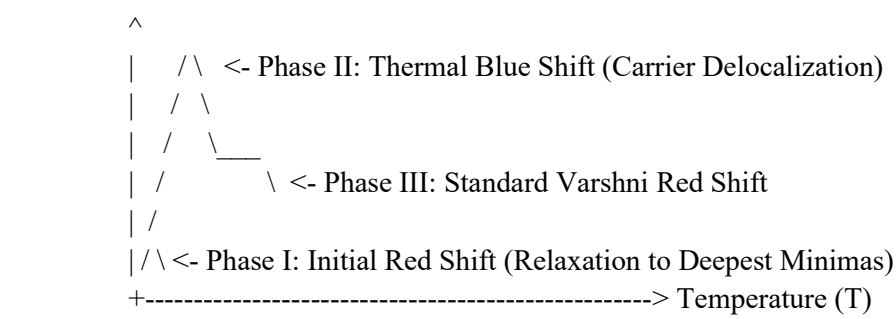

Figure 3 : The "S-Shaped" Thermal Peak Energy Trend

This S-shaped trend unfolds across three distinct thermal phases:

Phase I: Low Temperature (T < 70 K) – Initial Red Shift: At cryogenic temperatures, carriers are randomly distributed across various local potential energy states. As the temperature begins to rise slightly, carriers gain just enough thermal energy to escape from shallow localization sites.

They migrate through the continuous states and relax into the deepest available local potential wells before recombining radiatively. This redistribution concentrates the emission from lower-energy states, causing an initial red shift in the peak position that outpaces standard bandgap narrowing.

Phase II: Intermediate Temperature (70 K < T < 200 K) – The Blue Shift Turnaround: As the temperature rises further, the thermal kinetic energy (k_BT) approaches and exceeds the average localization depth (E_{loc}). Carriers gain sufficient energy to escape the local potential minima entirely, distributing themselves more uniformly across the extended, higher-energy states of the 2D quantum well subbands.

This delocalization process shifts the radiative transitions back to higher energy states, creating a distinct blue shift in the emission peak that opposes the underlying bandgap narrowing.

Phase III: High Operating Temperature (T > 200 K) – Standard Varshni Red Shift: Once the temperature surpasses the delocalization threshold, carriers behave like a hot, free-gas distribution within the extended subbands. In this high-temperature regime, individual localization effects become negligible.

The emission peak follows the standard monotonic red shift driven by lattice expansion and enhanced electron-phonon scattering, as modeled by Varshni's equation:

$$E_g(T) = E_g(0) - \frac{\alpha T^2}{T + \beta}$$

Concurrently: Thermal Screen Attenuation of QCSE: Operating conditions introduce an additional layer of complexity. When an LED is driven at high forward currents, the high density of injected electrons and holes creates a localized screening charge. This carrier accumulation generates an internal counter-field that shields the quantum wells, partially flattening the tilted bands caused by the QCSE. This screening action returns the wavefunctions to a more symmetric alignment, increasing radiative efficiency and causing an additional blue shift that modulates the thermal red-shift rate.

However, as the junction temperature rises, accelerated non-radiative recombination and carrier leakage reduce the steady-state carrier density (n, p) within the wells. This drop in carrier concentration weakens the screening effect, allowing the internal piezoelectric field to tilt the bands once more. This interaction accelerates the spectral red shift at elevated temperatures, requiring precise stabilization strategies in practical applications.

III: EXPERIMENTAL METHODOLOGY AND INSTRUMENTATION

3.1 Design of the Experimental Setup: To accurately characterize the emission spectra of light-emitting diodes under varying thermal conditions, the experimental architecture must isolate the effects of temperature from other compounding variables. In semiconductor optoelectronics, an LED's spectral signature is highly sensitive to both external ambient temperature and internal electrical excitation levels. Therefore, the testing apparatus must maintain strict control over environmental variables while capturing high-resolution optical data.

The experimental setup designed for this investigation isolates and regulates the thermal state of the LED under test while capturing real-time radiometric data. The physical system is divided into four integrated functional blocks:

1. The Isolated Thermal Control Environment
2. The Precision Electrical Excitation Engine
3. The Optical Collection and Transmission Couplings
4. The Centralized Data Acquisition and Orchestration System

3.1.1 The Isolated Thermal Control Environment: The core requirement of this experiment is the ability to vary the ambient temperature of the LED package systematically without introducing external light contamination or mechanical instability.

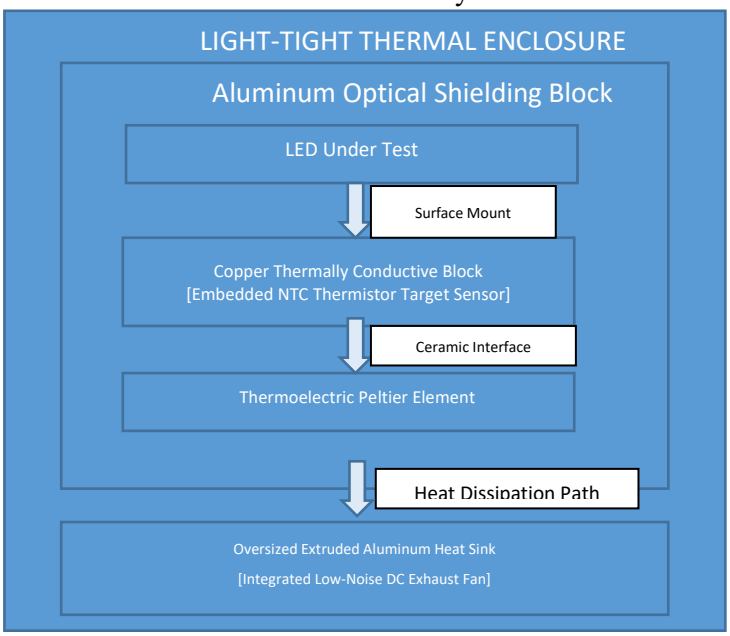

Figure 4: The Isolated Thermal Control Environment

1. **Physical Housing and Ambient Shielding:** The testing assembly is housed within a rigid, double-walled aluminum optical isolation enclosure. The interior surfaces are coated with a matte-black, non-reflective polyurethane paint designed to absorb stray reflections and eliminate scattered photons. This housing provides complete isolation from ambient room lighting, preventing background optical noise from contaminating the sensitive charge-coupled device (CCD) spectrometer arrays.
2. **The Multi-Layer Solid-State Heat Exchanger:** The temperature-regulation engine relies on a multi-layer solid-state assembly that provides dual-directional thermal control (heating and cooling):

a. **The Core Substrate:** The LED package is surface-mounted onto a custom-machined copper block ($k \approx 401$ W/m. K). Copper's high thermal conductivity ensures a uniform temperature distribution across the mounting interface, minimizing localized lateral thermal gradients.

b. **Thermoelectric Peltier Actuator:** The base of the copper block is coupled to a high-power bismuth telluride (Bi_2Te_3) Thermoelectric Cooler (TEC), or Peltier element. By controlling the direction and magnitude of the DC current injected into the TEC, the element acts as an active solid-state heat pump, either forcing thermal energy upward into the copper substrate to heat the LED or drawing heat downward to cool it.

c. **The Thermal Waste Sink:** The lower, hot-side plate of the Peltier element is clamped to an oversized extruded aluminum heat sink equipped with an active, low-noise DC exhaust fan. This assembly quickly dissipates excess thermal waste into the external environment, preventing thermal runaway when operating the system at low cryogenic or high sub-ambient target points.

d. Interface Optimization: Every physical junction within the stack is compressed under a uniform mechanical load ($P \approx 0.5$ MPa) and filled with an ultra-thin layer of synthetic silver-sintered thermal paste ($k >$ 8.5 W/m. K). This displaces microscopic air pockets and reduces the contact thermal resistance (\theta{contact) to negligible level**s.**

3.1.2 The Precision Electrical Excitation Engine: Because injection current density altered via self-heating can mimic or obscure purely thermal spectral shifts, the electrical drive sub-system must deliver high-stability power.

3.1.2.1. Constant Current Source Architectures: The electrical engine utilizes an automated, ultra-low-noise programmable DC current source capable of delivering continuous currents from 0.1 mA to 1.50 A with a setpoint resolution of ±10 μA. The driver employs a high-frequency, closed-loop operational amplifier feedback topology that monitors the load current across an internal high-precision manganese-copper shunt resistor. This architecture suppresses current fluctuations to less than 0.02% over extended testing intervals, ensuring that any observed modifications in photon emission density are driven strictly by the controlled thermal environment.

3.1.2.2. Pulsed-Current Modulation Capability: To differentiate between external ambient temperature effects and internal self-heating caused by power dissipation ($P_{diss} = I_F \cdot V_F$), the source is integrated with a solid-state MOSFET switching matrix. This allows the system to transition from continuous-wave (CW) mode to narrow-pulsed excitation modes.

The pulse generator can produce clean rectangular current pulses with widths (t{pulse) adjustable from 10 μ s to 1 ms and a duty cycle (D) of less than 1%. Using short pulse durations prevents carrier accumulation and heat generation within the active multi-quantum wells, allowing the p-n junction temperature to remain tightly locked to the calibrated temperature of the external copper block.

3.1.3 The Optical Collection and Transmission Couplings: The optical sub-system must collect emitted photons uniformly across a wide angular distribution and route them to the analyzing instrument without altering their spectral properties.

1. **The Cosine Corrector Interface:** At the collection point, light from the LED is captured by a specialized cosine corrector probe mounted at a fixed distance (d = 30 mm ±0.1 mm) and aligned perfectly with the optical axis of the semiconductor die. The cosine corrector contains a specialized, highly diffusing opaline silica disc that scatters incoming photons across a complete 180° angular field of view.

This optical diffusion yields an explicit spatial integration of the emission field. As an LED heats up, changes in its structural refractive indices can alter its spatial spatial radiation pattern (spatial lambertian distribution profile). The cosine corrector compensates for these spatial variations, ensuring that the collected light accurately reflects the device's total spectral output rather than localized directional shifts.

2. **Fiber Optic Routing Mechanics:** The output of the cosine corrector couples directly into a multi-mode fiber optic patch cord. The cable contains a high-purity fused silica core (D_{core} = 600 μm, Numerical Aperture NA = 0.22) enclosed in an armored stainless-steel jacket to resist thermal expansion when positioned near the heated stages. Fused silica exhibits a completely flat optical transmission attenuation coefficient across the entire visible spectrum (380 nm - 780 nm), guaranteeing that the fiber assembly introduces no chromatic aberration or wavelength-dependent wavelength filters before the signal reaches the spectrometer.

3.1.4 Centralized Data Acquisition and Orchestration System: To minimize human error and eliminate temporal drift during testing, all components are managed by a centralized digital orchestration matrix via an IEEE-488 General Purpose Interface Bus (GPIB) and high-speed USB links.

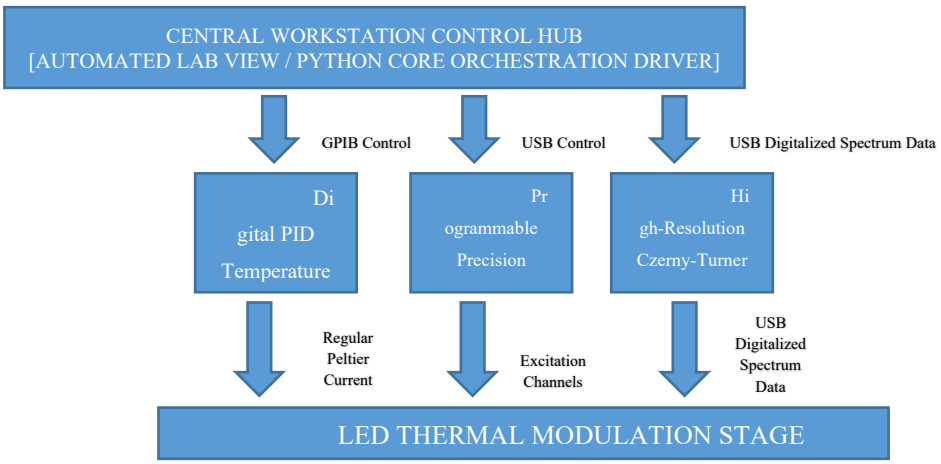

Figure 5: Centralized Digital Orchestration Matrix

The system automation runs on a custom script developed in a high-level programming language (such as Python or LabVIEW), which executes the following measurement loop:

1. **Thermal Step Adjustment:** The automation script issues a digital command to the PID controller, establishing the next target thermal checkpoint (e.g., T = 313.00 K).
2. **Thermal Equilibrium Monitoring:** The script monitors the NTC thermistor readings. The temperature must stabilize within a tight tolerance (± 0.05 K) for a continuous dwell period of 300 seconds to ensure the entire copper substrate, packaging base, and internal p-n junction reach complete steady-state thermal equilibrium.
3. **Excitation Triggering**: The precision current source is enabled at the target current parameter (I_F = 350 mA).
4. **Spectral Acquisition:** The fiber spectrometer triggers simultaneously, matching its integration time to the current intensity profile to capture data at optimal signal-to-noise ratios.
5. **Isolation Current Safety Close:** The excitation current is disabled immediately following data capture to minimize internal self-heating. The raw digitized spectrum, forward voltage drop (V_F), and thermistor temperature data are saved to disk before advancing to the next thermal step.

3.2 Temperature Control and Stabilization Mechanisms: To successfully isolate the effects of temperature on LED emission spectra, the experimental design must maintain steady-state thermal conditions at the microscopic p-n junction. In semiconductor testing, even a minor thermal fluctuation (± 0.5 K) can cause measurable wavelength drifts and intensity variations, compromising the integrity of the collected data.

To prevent these errors, this setup utilizes a high-precision, closed-loop thermal control system. This system combines solid-state thermoelectric heat pumping, digital proportional-integral-derivative (PID) modeling, and advanced thermal resistance calibration to regulate the device's temperature.

3.2.1 Thermoelectric Cooler (TEC) Physics and Operation: The core thermal actuator used in this setup is a solid-state Thermoelectric Cooler (TEC), also known as a Peltier module. The module consists of alternating pairs of heavily doped p-type and n-type Bismuth Telluride (Bi_2Te_3) semiconductor pellets arranged electrically in series and thermally in parallel. These pellets are sandwiched between two flat, electrically insulating ceramic substrates (typically Aluminum Oxide, Al_2O_3).

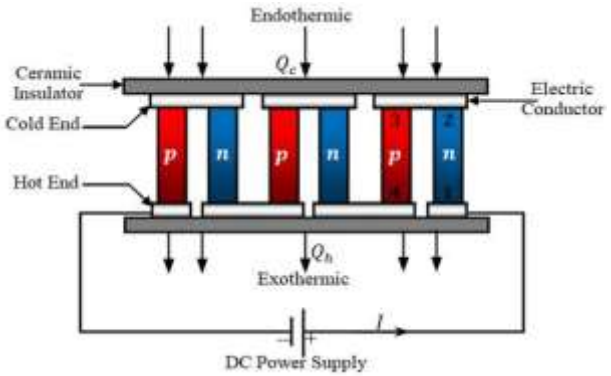

Figure 6: Cross-Section of a Solid-State Peltier (TEC) Element

The operation of the TEC relies on the Peltier Effect. When an external DC current (I_{tec}) flows through the junction of the dissimilar semiconductor pellets, it drives a heat flux from one ceramic plate to the other. At the cold junction, electrons absorb thermal energy as they transition from the lower energy levels of the p-type material to the higher valence states of the n-type material, lowering the plate's temperature. Concurrently, at the opposite junction, electrons release this accumulated energy, heating the hot-side plate.

The total heat absorption rate (Q{cold) at the active cooling interface is modeled by the following thermodynamic balance equation:

$$Q_{cold} = \pi_{ab} I_{tec} - \frac{1}{2} I_{tec}^2 R_{tec} - K_{tec} (T_{hot} - T_{cold})$$

Where π_{ab} is the differential Peltier coefficient between the semiconductor legs (a and b), which is directly related to the material Seebeck coefficient ($\alpha_{seebeck}$) by $\pi = \alpha_{seebeck} T$, R_{tec} is the internal electrical resistance of the module. The term $\frac{1}{2}I_{tec}^2R_{tec}$ represents internal Joule heating, which splits equally and flows toward both ceramic plates, opposing the cooling effect.

K_{tec} is the absolute thermal conductance of the module. The term K_{tec} (T_{hot} - T_{cold}) accounts for passive Fourier heat conduction leaking back from the hot plate to the cold plate through the semiconductor material.

By adjusting the polarity and magnitude of the drive current (I_{tec}), the module can transition seamlessly between heating and cooling modes. This dual-directional capability enables precise temperature regulation across the entire target testing range (283 K to 363 K).

3.2.2 High-Sensitivity Sensor Feedback Networks: To maintain high stability, the feedback network uses a miniature, glass-encapsulated Negative Temperature Coefficient (NTC) thermistor (10 kΩ ± 0.1% tolerance at 298.15 K). The thermistor is embedded within a custom-drilled channel in the copper mounting block, positioned within 1 mm of the LED package's thermal pad.

The electrical resistance (R) of an NTC thermistor decreases exponentially as temperature increases. This relationship is modeled precisely over wide thermal spans using the Steinhart-Hart equation:

$$\frac{1}{T} = A + B \ln (R) + C (\ln (R))^3$$

Where T is the absolute temperature in Kelvin, and A, B, and C are empirical curve-fitting constants calculated during factory calibration against standard platinum resistance thermometers (PRTs).

The thermistor is biased by a filtered, low-drift reference current source (I_{bias} = 100 μA). The resulting analog voltage drop is digitized by a high-resolution 24-bit Delta-Sigma (ΔΣ) Analog-to-Digital Converter (ADC) that includes built-in 50 Hz/60 Hz power-line noise rejection filters. This high-resolution acquisition network detects temperature variations as small as ±0.005 K, providing a clean feedback signal for the control system.

3.2.3 Digital PID Control Algorithms: The digitized temperature signal is routed to a dedicated digital microprocessor running a closed-loop Proportional-Integral-Derivative (PID) control algorithm. The algorithm continuously calculates a thermal error signal, e(t), which represents the difference between the user's target setpoint (T_{set}) and the current measured temperature ($T_{meas}(t)$):

$$e(t) = T_{set} - T_{meas}(t)$$

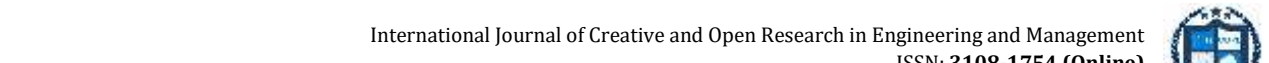

The controller computes the required output current command, u(t), sent to the TEC bipolar H-bridge power stage using three parallel mathematical operations:

$u(t) = K_p\, e(t) + K_i \int_0^t e_\tau \, d\tau + K_d \frac{de(t)}{dt}$

Each parameter manages a distinct aspect of the system's thermal response:

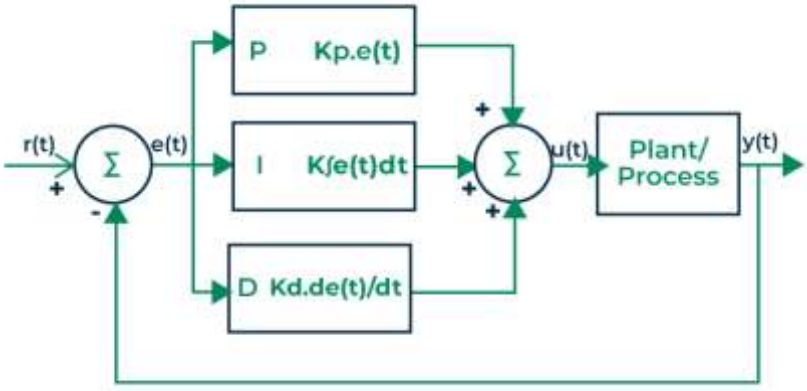

Figure 7: Functional Architecture of the PID Loop

1. **The Proportional Term (K_p):** Generates an output response proportional to the immediate magnitude of the error signal. A higher gain increases response speed but can cause system oscillations if set too high.
2. **The Integral Term (K_i):** Integrates the error over time to eliminate any steady-state thermal offset caused by continuous ambient heat loads. To prevent integral windup—where large setpoint changes create massive current overshoots—the integration term is constrained by software anti-windup clamping limits.
3. **The Derivative Term (K_d):** Monitors the rate of change of the error signal, predicting future temperature variations. This term acts as an electronic brake, dampening oscillations and suppressing overshoots when approaching the target temperature.

The loop coefficients were optimized using the Ziegler-Nichols tuning method, followed by manual fine-tuning to account for the thermal mass of the copper block. This configuration stabilizes the copper stage within \pm 0.02 K of the target setpoint under steady-state conditions.

3.2.4 Real-Time Junction Temperature Matrix Adjustments: While the PID loop tightly regulates the external copper mounting block (T_b), the temperature at the active p-n junction (T_j) will always be higher under continuous operating currents (I_F). This temperature difference is caused by the internal thermal resistance of the LED package (θ_{jc}), which impedes heat flow away from the semiconductor die.

To track this internal heating, the system uses a dual interface transient calibration protocol (JEDEC JESD51-1) to calculate T_j in real time. The steady-state heat flux (Q_{heat}) generated by the LED equals the electrical input power minus the emitted optical power:

$Q_{heat} = P_{electrical} - P_{optical} = (I_F . V_F) - \int S_{corrected}\,(\lambda)\, d\lambda$

The actual junction temperature is then calculated dynamically using the following thermal resistance network equation:

$T_j = T_{meas} + Q_{heat}\,(\theta_{junction\text{-}case} + \theta_{interface})$

Where $\theta_{junction\text{-}case}$ is the fixed internal resistance of the LED package, and $\theta_{interface}$ is the calibrated contact resistance of the thermal paste interface.

Before recording an optical spectrum, the automated software checks both the external thermistor stability and the calculated internal junction temperature (T_j). The system must maintain a stable thermal profile ($\pm$ 0.05 K) for a continuous 300-second dwell period to ensure complete steady-state thermal equilibrium across all layers before data acquisition begins.

3.3 Optical Measurement and Spectroradiometric Instrumentation: Capturing the subtle modifications of an LED's emission spectrum under varying thermal loads requires an optical collection and detection system

with high resolution, excellent throughput, and repeatable geometric alignment. Because thermal shifts in advanced materials like InGaN can be as small as +0.045 nm/K, the measurement instrumentation must isolate the true spectral signature from systemic distortions, stray light, and detector non-linearities.

The spectro-radiometric system developed for this study relies on a precise optical train. This setup routes emitted photons from the active p-n junction through an integrating input interface, a fiber transmission link, and a high-resolution diffraction spectrometer before digitizing the signal with a calibrated sensor array.

3.3.1 Geometric Alignment and Light Collection Interfaces: The first critical step in spectroradiometry is matching the collection optics to the spatial radiation pattern of the LED. As an LED's junction temperature rises, its internal refractive indices change. These thermal modifications alter the chip's spatial emission profile, distorting the directional intensity distribution. If a standard lens system is used, these spatial variations can mimic or obscure true spectral changes.

To eliminate this source of error, this setup replaces traditional directional imaging lenses with a precision Cosine Corrector. This collection probe is mounted at a fixed distance (d = 30 mm ±0.1 mm) along the central optical axis of the LED package. The corrector features a specialized 6 mm diameter diffusing disc machined from ultra-pure, non-fluorescent opaline silica.

The physical structure of the opaline disc scatters incoming light rays, providing a uniform spatial integration that matches a true cosine response:

$I_\theta = I_0 \cos \theta$

Where \theta is the angle of incidence relative to the surface normal. By collecting and integrating photons across a full 180^o angular field of view, the cosine corrector ensures that the recorded signal represents the device's total integrated spectral distribution, isolating the data from localized directional shifts or beam steering caused by thermal expansion.

3.3.2 Fiber Optic Waveguide Transmission Mechanics: Once integrated by the cosine corrector, the light is routed to the spectrometer through a high-performance multi-mode fiber optic patch cable. The fiber assembly uses a Step-Index Optic Design optimized for visible spectrum transmission, featuring the following technical specifications:

Component / Parameter	**Specification / Material**
Core Material	High-Purity Fused Silica (SiO_2)
Cladding Material	Fluorine-Doped Silica Glass
Core Diameter ($\mathbf{D_{core}}$)	600 µm ± 5 µm
Numerical Aperture (**NA**)	0.22 ± 0.01
Acceptance Cone Angle ($\mathbf{2\theta}$)	$\approx 25.4^0$
Mechanical Sheathing	Interlocking Armored Stainless Steel

The high-purity fused silica core features an ultra-low attenuation profile (α attenuation < 10 dB/km) across the entire visible wavelength range (380 nm - 780 nm). This flat response guarantees that the fiber optic link introduces no artificial spectral weighting or chromatic filtering. The armored stainless-steel sheathing provides rigid structural protection, preventing micro-bending losses and maintaining a fixed internal reflection geometry during thermal cycling.

3.3.3 The Czerny-Turner Spectrometer Architecture: The core component of the optical instrumentation is a high-resolution spectrometer based on an asymmetric Czerny-Turner Optical Configuration. This design provides excellent optical resolution and minimizes internal stray light reflections within a compact physical footprint.

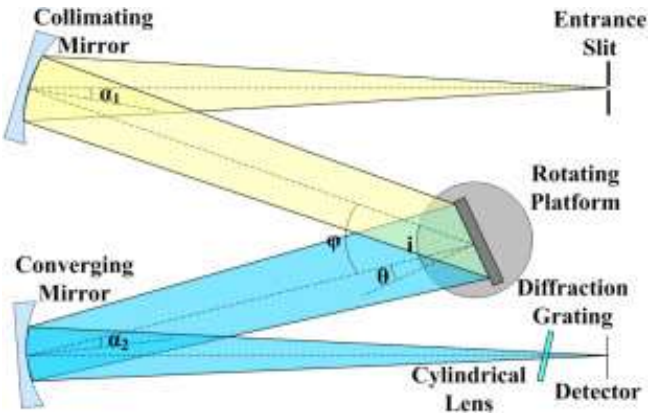

Figure 8: Asymmetric Czerny-Turner Spectrometer Layout

The optical path within the Czerny-Turner spectrometer consists of five functional stages:

1. **The Entrance Slit Interface:** Light from the fiber patch cable enters the instrument through a high-precision, laser-etched air slit with a fixed width of 25 μm. The narrow slit width acts as a spatial filter, defining the minimum achievable optical resolution (λλ{res) of the system.
2. **Collimating Reflection Optics:** The diverging light beam from the entrance slit strikes a front-surface off-axis parabolic mirror. The mirror features an ultra-flat gold/aluminum reflective coating (R > 92\%), aligning the divergent rays into a perfectly parallel, collimated beam directed toward the dispersive element.
3. **Planar Diffraction Grating Dispersion:** The collimated beam hits a planar reflection diffraction grating. The grating features a high groove density of 1200 lines/mm, which is blazed at an optimal angle of 500 nm to maximize first-order diffraction efficiency across the visible spectrum. The grating splits the composite white or monochromatic light into angularly separated wavelengths according to the fundamental grating equation:

$m\lambda = d(\sin \alpha_{in} + \sin \beta_{out})$

where m is the diffraction order (m = 1), d is the groove spacing (1/1200 mm ≈ 833.3 nm), α_{in} is the fixed angle of incidence, and β_{out} is the wavelength-dependent angle of diffraction.

4. **Focusing Projection Mirrors:** The angularly dispersed beams hit a second front-surface focusing mirror. This mirror focuses each individual wavelength band onto a specific spatial coordinate along the exit focal plane.
5. **Linear CCD Array Detection:** The focused spectral image is captured by a high-sensitivity linear Charge-Coupled Device (CCD) sensor array located at the exit focal plane. The detector features 2048 individual pixel elements arranged in a horizontal line, with each pixel measuring 14 μm x 200 μm. This high pixel density maps the visible spectrum at an exceptional dispersion ratio of 0.2 nm/pixel, providing a true system optical resolution of $FWHM_{res}$ = 0.5 nm.

3.3.4 CCD Integration Control and Electronic Digitization: The pixel array converts incoming photons into digital counts via a multi-stage electronic digitization sequence. When a photon strikes a pixel's active silicon layer, it generates an electron-hole pair through the photoelectric effect. These photo-generated electrons collect within the pixel's localized potential well during a controlled integration interval (t_{int}).

To maintain accuracy across varying thermal states, the integration time is managed by an automated software loop:

- At high temperatures or lower conversion efficiencies, the integration time is extended (up to 500 ms) to accumulate more charge and maximize the signal-to-noise ratio (SNR).
- At highly efficient low-temperature points, the integration time is reduced (down to 10 ms) to prevent charge overflow, or pixel saturation.

Once the integration window closes, the accumulated charge packets are shifted out of the array into a low-noise pre-amplifier stage. The amplified analog signals are then converted into digital data by a high-resolution 16-bit Analog-to-Digital Converter (ADC). This converter resolves individual pixel intensities across 65,536 discrete

digital counts (0 to 65,535 Counts), providing the precision needed to track small variations in spectral shape and peak positions.

3.4 Calibration and Data Processing Procedures: To convert the raw electronic counts generated by a 16-bit linear CCD array into physically meaningful, metrologically traceable spectroradiometric data, a rigid sequence of calibration and data processing must be executed. Raw data from a diffraction spectrometer contains structural errors introduced by variations in pixel layout, non-uniform optical transmission across different wavelengths, detector dark currents, and high-frequency electronic noise.

The mathematical framework and calibration protocols detailed below isolate the true optical emission profile of the LED under test, ensuring that subsequent extractions of peak wavelengths (λ_p), linewidths ($\Delta\lambda_{FWHM}$), and integrated optical powers are highly accurate.

3.4.1 Wavelength Calibration Protocol (Pixel-to-Wavelength Mapping): The position of a specific pixel in a linear CCD array does not inherently correspond to an absolute optical wavelength. The diffraction angle (β_{out}) from a planar reflection grating varies non-linearly across the flat face of the sensor array. Therefore, a spatial-to-spectral calibration must be established.

This calibration is performed using a certified low-pressure Helium-Neon (HeNe) and Argon (Ar) gas discharge reference lamp. These gas discharge sources produce highly stable, atomic emission lines at precise, universally verified wavelengths determined by electronic orbital transitions.

The calibration sequence involves the following steps:

1. The discharge lamp is positioned at the entrance interface of the cosine corrector.
2. A high-resolution scan is captured, identifying the exact pixel indices (p) where the peak intensities of the known reference lines occur.
3. A third-order polynomial regression equation is fitted to the data points using a least-squares algorithm to map the pixel index (p) to its absolute corresponding wavelength (λ):

$$\lambda(p) = a_0 + a_1 p + a_2 p^2 + a_3 p^3$$

where p is the integer pixel index ($1 \leq p \leq 2048$), a_0 is the intercept coefficient, representing the theoretical baseline wavelength of the first pixel element, a_1, a_2 and a_3 are regression coefficients that account for the linear dispersion ratio and the non-linear optical aberrations across the exit focal plane.

4. Following calibration, the residual error across the entire visible spectrum (380 nm - 780 nm) is constrained to less than ± 0.05 nm, providing the precision required to track subtle thermal wavelength shifts.

3.4.2 Relative Radiometric Calibration (Spectral Sensitivity Correction): Even after accurate wavelength mapping, the raw intensity counts recorded by individual pixels do not reflect the true proportional balance of photons across the spectrum. Every optical component inside the Czerny-Turner spectrometer introduces a wavelength-dependent modification:

- The silica core of the fiber optic cable exhibits increased attenuation at shorter UV/blue wavelengths.
- The diffraction efficiency of the blazed reflection grating peaks at 500 nm and drops toward the red and violet ends of the spectrum.
- The quantum efficiency (η_{QE}) of the silicon CCD array is highly efficient between 500 nm - 650 nm but falls off sharply as it approaches the silicon bandgap limit in the near-infrared 1100 nm.

To compensate for these system variations, a Relative Radiometric Calibration is performed using a certified NIST-traceable Tungsten-Halogen standard lamp. This reference lamp operates under a highly stabilized current configuration, emitting a continuous spectral irradiance profile that closely matches a theoretical blackbody radiator at a known color temperature ($T_{color} \approx 3100$ K), as defined by Planck's law:

$$I_{ideal}(\lambda) = \frac{2hc^2}{\lambda^5} \frac{1}{\exp\left(\frac{hc}{\lambda k_B T}\right) - 1}$$

During calibration, the standard lamp's known spectral output, $I_{ideal}(\lambda)$, is compared against the raw digital intensity counts, $S_{standard,\ raw}(\lambda)$, recorded by the spectrometer. This comparison is used to calculate a unique Spectral Correction Factor, **R(λ)**, for every wavelength coordinate:

$$R(\lambda) = \frac{S_{standard,raw}(\lambda) - S_{dark}(\lambda)}{I_{ideal}(\lambda) \cdot t_{calibration}}$$

Where $t_{calibration}$ is the integration time used during calibration. This arrays of correction parameters acts as an inverse sensitivity filter, correcting the raw data captured during subsequent LED testing.

3.4.3 Mathematical Noise Reduction and Preprocessing Flow: During an active measurement sequence at a specific junction temperature (T_j), the raw digitized signal, $S_{raw}(p)$, undergoes a multi-stage mathematical preprocessing sequence to eliminate electronic and environmental noise.

Step 1: Dark-Current Subtraction: Silicon CCD detectors are prone to thermal noise, where ambient thermal energy excites valence electrons into the conduction band independent of incoming photons. This creates an artificial background baseline known as dark current. Because dark current accumulates linearly over time, its effects become more pronounced during the longer integration intervals required at high temperatures.

To isolate and eliminate this error, a dark frame, $S_{dark}(p)$, is captured immediately prior to every active measurement by keeping the excitation current disabled while maintaining the target junction temperature. This background frame is subtracted directly from the active measurement:

$S_{net}(p) = S_{raw}(p) - S_{dark}(p)$

Step 2: Normalization for Integration Time and Sensitivity Filtering: The dark-corrected signal is then normalized relative to its specific integration window (t_{int}) and processed through the calibrated spectral correction matrix, $R(\lambda)$, generated in Section 3.4.2:

$S_{corrected}(\lambda) = S_{net}(p(\lambda)t_{int} \cdot R(\lambda)$

This step yields a corrected relative intensity spectrum, $S_{corrected}(\lambda)$, measured in units proportional to absolute spectral irradiance (Counts /s- μW).

3.4.4 Digital Signal Processing via Savitzky-Golay Filtering: Even after dark subtraction and radiometric correction, the raw spectrum can retain high-frequency electronic noise from the pre-amplifier and the high-resolution ADC. To smooth the curve without distorting critical peak parameters, the system uses a digital Savitzky-Golay Smoothing Filter.

Standard moving-average filters smooth data by averaging points within a moving window. However, this simple averaging can flatten sharp spectral peaks and artificially widen measured linewidths ($\Delta\lambda_{FWHM}$). The Savitzky-Golay method avoids this issue by fitting a local polynomial to the data points within a moving window using a linear least-squares algorithm.

For a targeted data point at wavelength index i, a localized symmetric window of size 2M + 1 is sampled:

$y = [S_{corrected}(\lambda_{i-M}). S_{corrected}(\lambda_i). S_{corrected}(\lambda_{i+M})]^T$

A second-order polynomial (k = 2) is fitted across this window:

$f(\lambda) = c_0 + c_1 \lambda + c_2 \lambda^2$

The coefficients (c_n) are calculated efficiently by multiplying the data vector by a matrix of pre-computed convoluting weights (C):

$c = (A^T A)^{-1} A^T y$

Where A is the local design matrix defined by the window configuration. The smoothed value for the central pixel is then set directly to the evaluated polynomial value:

$S_{smoothed}(\lambda_i) = c_0$

Using a balanced configuration (a 7-point window size, M = 3, combined with a second-order polynomial) suppresses high-frequency electronic noise by more than 15 dB. Crucially, this optimization maintains the true peak position (λ_p) and preserves the asymmetric line shape of the spectrum, providing clean data for subsequent parameter extraction.

3.4.5 Automated Extraction of Critical Spectral Parameters: Once the smoothed spectrum, $S_{smoothed}(\lambda)$, is generated, an automated algorithm extracts three critical optoelectronic parameters:

I. Peak Wavelength (λ_p) Extraction: Rather than selecting the single pixel with the highest intensity count—which is limited by the spectrometer's pixel dispersion resolution (0.2 nm)—the algorithm uses a local parabolic peak-fitting method.

The software identifies the absolute maximum point in the array and samples a narrow 5-point window centered around it. A second-order parabola is fitted to these five points:

$y(\lambda) = A\lambda^2 + B\lambda + C$

Differentiating this equation and setting it to zero gives the peak position with sub-pixel resolution:

$\frac{dy}{d\lambda} = 2A\lambda + B = 0 \Rightarrow \lambda_p = -B\{2A$

This fitting method calculates the peak position to within ± 0.01 nm, allowing the system to track subtle changes in bandgap narrowing.

II. Full-Width at Half-Maximum ($\Delta\lambda_{FWHM}$) Extraction: The algorithm extracts the linewidth by locating the maximum intensity ($I_{max} = S_{smoothed}(\lambda_p)$) and scanning outward in both directions to find the two half-power coordinates (λ_1 and λ_2) where the intensity drops to exactly half of the peak value:

$S_{smoothed}(\lambda_1) = S_{smoothed}(\lambda_2) = 0.5 \ . \ I_{max}$

Because these precise intensity values rarely align perfectly with a discrete pixel coordinate, the software uses linear interpolation between the two closest bounding pixels to pinpoint λ_1 and λ_2. The absolute linewidth is then calculated as:

$\Delta\lambda_{FWHM} = \lambda_2 - \lambda_1$

III. Integrated Optical Power (P_{opt}) Calculation: The total relative optical power is calculated by integrating the area under the corrected, smoothed spectral curve across the entire visible band emission window using Simpson's Composite Numerical Integration Rule:

$$P_{opt} = \int_{\lambda_{end}}^{\lambda_{start}} S_{smoothed}\ (\lambda)d\lambda \approx \frac{\Delta\lambda_{step}}{3}[S(\lambda_0) + 4\sum_{j=1}^{N/2} S(\lambda_{2j-1}) + 2\sum_{j=1}^{N/2} S(\lambda_{2j}) + S(\lambda_N)]$$

where $\Delta\lambda_{step}$ is the average wavelength spacing between adjacent pixels. This integrated value is recorded at each controlled temperature checkpoint, providing the quantitative data needed to model thermal quenching curves and evaluate internal efficiency drops.

3.5 Junction Temperature Determination Methods: In semiconductor optoelectronics, the temperature of the active microscopic p-n junction (T_j) cannot be measured directly using standard mechanical probes. Placing a physical thermistor or thermocouple directly onto the micron-scale semiconductor die is impossible because it would block the optical emission path, damage the wire bonds, and distort the local thermal field due to the probe's thermal mass. Furthermore, measuring only the temperature of the external copper mounting block (T_b) or package case (T_c) is insufficient because internal thermal resistance creates a significant temperature gradient under continuous driving currents.

To overcome this limitation, this study utilizes two independent, calibrated methods to determine Tj in real time: the Forward Voltage ($\mathbf{V_F}$) Temperature-Coefficient Method (an electrical electrical parameter technique) and the Steady-State Thermal Resistance Network Model.

3.5.1 Method A: The Forward Voltage (V_F) Temperature-Coefficient Method: The forward voltage drop across an LED's p-n junction under a forward bias current is highly temperature-dependent. When an LED is driven by a small, constant sensing current (I_{sense}), its forward voltage drops linearly as temperature increases. This predictable electrical behavior serves as an internal thermometer, providing a direct measurement of the junction temperature.

I. Physical and Semiconductor Mechanics: The relationship between current and voltage in a forward-biased ideal p-n junction is modeled by the Shockley diode equation:

$$I_F = I_s\left[\exp\left(\frac{qV_F}{n_{ideal}k_BT_j}\right) - 1\right] \approx I_s \exp\left(\frac{qV_F}{n_{ideal}k_BT_j}\right)$$

Where I_s is the reverse saturation current, q is the elementary electron charge, n_{ideal} is the ideality factor, and k_B is the Boltzmann constant. The reverse saturation current I_s is highly dependent on temperature because it scales with the intrinsic carrier concentration (ni^2):

$$Is \propto ni^2 \propto T_j^3 \exp\left(\frac{-E_g(T_j)}{k_BT_j}\right)$$

Substituting this temperature-dependent relationship back into the core diode equation, taking the natural logarithm, and differentiating with respect to temperature (dV_F / dT_j) under a fixed, low current yields a linear relationship:

$$\frac{dV_F}{dT_j} = -\frac{1}{T_j}\left[V_F(Tj) - \frac{E_g(0)}{q} \right] - \frac{3n_{ideal}\, k_B}{q} + \frac{1}{q}\frac{dEg}{dTj} \equiv kV$$

where kV is the temperature calibration coefficient (typically ranging from -1.5 mV/K to -2.5 mV/K depending on the semiconductor material). Because this coefficient remains highly linear across the standard operating range (283 K to 363 K), it can be used to track internal temperature variations.

II. The Calibration Sequence: Before conducting active spectral testing, a calibration run must be completed to determine the device's specific kV coefficient:

1. The LED is mounted to the copper stage inside the isolated thermal enclosure.
2. The programmable current source is set to a low, non-heating sensing level: I_{sense} = 1.00 mA. At this low current, the electrical power dissipation ($P_{elec} \approx 2.5$ mW) is too low to cause internal self-heating, ensuring the junction temperature (T_j) remains locked to the regulated base temperature (T_b).
3. The digital PID controller steps the temperature from 283.15 K to 363.15 K in precise 10.00 K increments.
4. At each checkpoint, after a 300-second stabilization window, a high-resolution digital multimeter records the steady-state forward voltage drop ($V_{F,sense}$).
5. The resulting voltage values are plotted against the calibrated thermistor temperatures, and a linear regression line is fitted to the data to extract the slope (kV):

$$V_F(T_j) = V_F(T_0) + kV \cdot (T_j - T_0)$$

III. Real-Time Pulsed Thermal Sampling Execution: Once kV is extracted, the system can measure the true junction temperature (T_j) during high-current continuous-wave (CW) testing (I_{drive} = 350 mA) using a rapid pulse-switching protocol.

1. The LED is driven at its continuous testing current (I_{drive} = 350 mA). The device heats up internally due to power dissipation.
2. Every 10 seconds, the automated software triggers the fast switching matrix, dropping the current from 350 mA down to the 1 mA sensing level (I_{sense}) for a brief sampling window (t_{sample} = 20 µs).
3. The multimeter records the voltage drop ($V_{F,sense}$) within this 20 µs window. The window is short enough that the junction does not cool down to the ambient base temperature during the measurement, capturing the true thermal state of the active region.
4. The current returns to 350 mA, and the software calculates the absolute junction temperature (T_j) using the calibrated coefficient.

3.5.2 Method B: The Steady-State Thermal Resistance Network Model: To validate the electrical measurements from Method A, this study uses a second independent approach based on thermal physics: a Steady-State Thermal Resistance Network Model that adheres to JEDEC JESD51 standards.

I. Electrical-Thermal Analogies and Flow Formulations: Heat transfer through an LED package behaves similarly to electrical current flowing through a resistive circuit. In this analogy, thermal energy flows from the high-temperature p-n junction (T_j) down through the package layers to the cooler external heat sink (T_b), driven by the structural temperature gradient.

Active Junction Region (Tj)

$R\theta_{junction\text{-}case}$ (Internal Package Resistance)

Package Substrate Base (Tc)

$R_{\theta case\text{-}board}$ (Solder Interface Resistance)

Metal-Core PCB Layer (Tb)

$R_{\theta board\text{-}ambient}$ (Heat Sink System Resistance)

Ambient Environment Target Room (Ta)

Figure 9: Layered Thermal Resistance Network

The mathematical equations governing this thermal flow are analogous to Ohm's Law:

Thermal Parameter	Electrical Analogy	Formulations Mapping
Temperature Diff. (Δ**T**)	Voltage Drop (V)	$\Delta T = T_{source} - T_{sink}$
Thermal Heat Dissipation ($\mathbf{Q_{th}}$)	Current Flow (I)	$Q_{th} = P_{electrical} - P_{optical}$
Thermal Resistance ($\mathbf{R_\theta}$)	Electrical Resistance (R)	$R_\theta = \Delta T / Q_{th}$ (K/W)

Table 1 : . Electrical-Thermal Analogies

II. Isolating the Thermal Heat Dissipation (Q_{th}): The total heat flux (Q_{th}) flowing through the package layers does not equal the total electrical input power ($I_F.V_F$). Instead, a portion of that electrical energy is converted into light and escapes the system as photons.

To determine the true heat flux, the total emitted optical power must be integrated and subtracted from the electrical input:

$$Q_{th} = P_{electrical} - P_{optical} = (I_F.\ V_{F,drive}) - \int_{\lambda_{start}}^{\lambda_{end}} S_{smoothed}(\lambda)d\lambda$$

where $V_{F,drive}$ is the active forward voltage under high current, and the integral calculates the total absolute optical power from the processed spectrum.

III. Calculating Tj from the Resistance Stack: Once Q_{th} is isolated, the junction temperature is determined by multiplying the heat flux by the total thermal resistance of the path and adding the temperature measured at the baseline thermistor (T_b):

$$T_j = T_b + Q_{th} .\ (R_{\theta,junction\text{-}case} + R_{\theta,case\text{-}board})$$

Where $R_{\theta,junction\text{-}case}$ is the internal thermal resistance from the p-n junction to the bottom thermal pad of the package, supplied by the device manufacturer & $R_{\theta,case\text{-}board}$ is the interface thermal resistance of the solder and silver-sintered thermal paste layer, pre-calibrated using transient dual-interface testing (JEDEC JESD51-14).

During testing, the software compares the T_j values calculated by Method A and Method B in real time. If the two values diverge by more than ±0.4 K, it indicates a potential calibration drift or a change in the interface thermal resistance. The system will automatically pause testing and run a recalibration sequence before resuming data collection, ensuring high accuracy across all operating states.

IV: EXPERIMENTAL RESULTS AND IN-DEPTH DISCUSSION

This Part presents the core empirical findings of this investigation, providing a detailed analysis of the experimental data collected across three distinct light-emitting diode architectures: monochromatic Indium Gallium Nitride (InGaN) blue LEDs, monochromatic Aluminum Gallium Indium Phosphide (AlGaInP) red LEDs, and phosphor-converted white LEDs (pc-WLEDs).

All devices were evaluated under steady-state thermal conditions ranging from 283 K to 363 K (10℃ to 90℃) in 10 K increments. To maintain consistency, measurements were recorded at a constant forward driving current (I_F = 350 mA) using the pulsed thermal sampling protocols detailed in Part 3 to isolate true thermal effects from internal self-heating.

4.1 Characterization of Blue InGaN LEDs: The first evaluation focused on commercial InGaN multi-quantum well (MQW) blue LEDs grown on a sapphire substrate. This material system forms the backbone of modern short-wavelength solid-state optoelectronics.

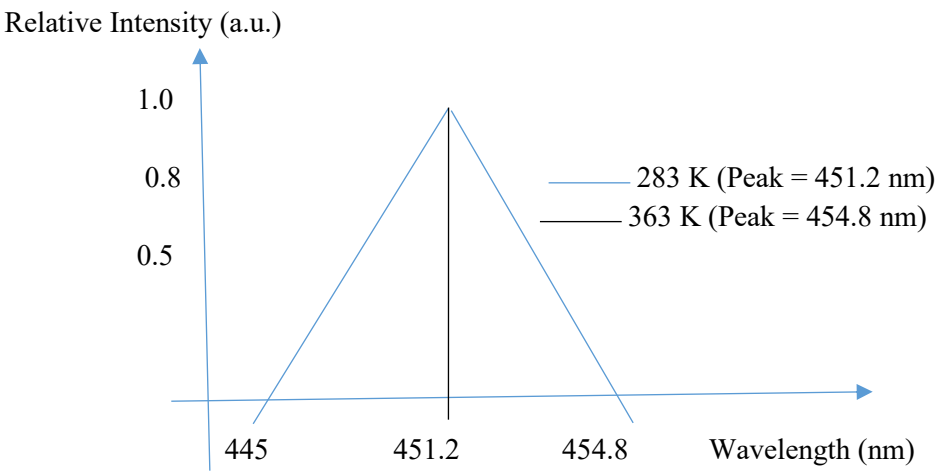

Figure 10. Thermally Induced Red Shift in Blue InGaN LEDs (350 mA)

4.1.1 Peak Wavelength Drifts and Bandgap Narrowing Analysis: At the initial base temperature of 283 K, the blue InGaN LED exhibits a sharp, symmetric emission profile centered at a peak wavelength (λ_p) of 451.2 nm (2.748 eV). As the controlled junction temperature (T_j) increases to 363 K, the emission peak systematically moves to 454.8 nm (2.726 eV). This indicates a net red shift of +3.6 nm over the 80 K thermal window, yielding an average temperature shift coefficient of:

$$\frac{d\lambda_p}{dT} \approx +0.045 \text{ nm/K}$$

This red shift is primarily driven by thermally induced bandgap narrowing within the ternary $In_xGa_{1-x}N$ quantum wells. Converting the peak wavelengths into photon energies ($E_p = \frac{hc}{\lambda_p}$) and plotting them against temperature allows the data to be fitted to Varshni's semi-empirical model:

$$E_g(T) = E_g(0) - \frac{\alpha T2}{T + \beta}$$

The mathematical fit extracts the following material parameters for the active layer:

- Extrapolated Bandgap at absolute zero (**$E_g(0)$**): 2.795 eV
- Lattice-Phonon Coupling Coefficient (**α**): 5.8 \times 10^{-4 eV/K
- Debye-Related Material Constant **(β)**: 600 K

These parameters match verified values for high-brightness GaN heterostructures. The relatively small shift coefficient highlights the structural rigidity of the group-III nitride crystal lattice, which resists significant thermal expansion across this temperature range.

4.1.2 Spectral Linewidth Broadening Mechanisms: The full-width at half-maximum ($\Delta\lambda_{FWHM}$) of the InGaN emission spectrum exhibits a linear increase with temperature, expanding from 18.4 nm (112 meV) at 283 K to 23.1 nm (139 meV) at 363 K. This broadening rate follows the theoretical relationship derived from Maxwell-Boltzmann carrier distributions ($\Delta E \approx 1.8\ k_B\ T$).

However, the experimental linewidth includes an additional structural broadening component (45 meV) that remains constant across all temperatures. This constant baseline is caused by inhomogeneous broadening, which stems from localized variations in Indium composition and small thickness fluctuations within the nanometer-scale quantum wells introduced during epitaxial growth.

At elevated temperatures, the high-energy (short-wavelength) tail of the spectrum extends outward, shifting the overall profile into an asymmetric shape. This tailing occurs because the high thermal energy (k_BT) distributes injected electrons and holes into higher-energy states within their respective subbands before they undergo radiative recombination.

4.1.3 Thermal Quenching of Internal Efficiency: The integrated optical power—calculated by summing the area under the corrected spectral curve—declines steadily as temperature increases. At 363 K, the absolute optical output power drops to 84.2% of the baseline value recorded at 283 K.

This drop is caused by thermal quenching of the internal quantum efficiency (IQE). As the crystal lattice heats up, increased lattice vibrations enhance electron-phonon scattering. This interaction accelerates non-radiative Shockley-Read-Hall (SRH) recombination, trapping charge carriers in deep-level crystal defects before they can recombine radiatively.

4.2 Characterization of Red AlGaInP LEDs: To contrast with the nitride system, high-power quaternary Aluminum Gallium Indium Phosphide $(Al_{0.5}Ga_{0.5})_{0.5}In_{0.5}P$ red LEDs were evaluated under identical environmental conditions.

4.2.1 Accelerated Red Shift and Material Sensitivity: The red AlGaInP devices show a much higher sensitivity to temperature variations than the blue InGaN structures. At 283 K, the red LED emits a narrow spectrum centered at 621.5 nm (1.995 eV). When heated to 363 K, the peak wavelength shifts to 634.1 nm (1.955 eV). This represents a red shift of +12.6 nm over the same 80 K span, resulting in a calculated temperature coefficient of:

$$\frac{d\lambda_P}{dT} \approx +0.157 \text{ nm/K}$$

This shift coefficient is more than three times larger than that of the blue InGaN LED. This high thermal sensitivity is an inherent characteristic of the phosphide alloy system.

Phosphide crystals exhibit a lower Debye temperature ($\theta_D \approx 400$ K) and a weaker lattice bonding energy than nitrides. Consequently, increasing the temperature causes larger changes in interatomic spacing, which accelerates lattice expansion and leads to a more rapid drop in the fundamental bandgap energy (E_g).

4.2.2 Linewidth Alterations and High-Energy Tail Spreading: The spectral linewidth of the AlGaInP device widens from $\Delta\lambda_{FWHM} = 14.2$ nm at 283 K to 20.8 nm at 363 K. Because the initial material distribution is more uniform, the red LED exhibits much less inhomogeneous broadening at low temperatures than the InGaN device. However, its thermal broadening rate is steeper.

The high-energy side of the spectrum spreads out rapidly at higher temperatures. This severe tailing indicates that carriers easily gain kinetic energy within the relatively light effective mass states of the AlGaInP conduction band, allowing them to occupy a wider range of high-energy levels before recombining.

4.2.3 Severe Thermal Quenching and Confinement Barrier Leakage: The most significant degradation observed in the AlGaInP LED is the rapid loss of optical power. When heated to 363 K, the integrated optical power drops sharply, retaining only 51.4% of its initial value at 283 K.

This severe thermal quenching is caused by carrier leakage over the heterostructure confinement barriers. In red phosphide LEDs, the conduction band offset (ΔE_c) between the AlGaInP quantum wells and the adjacent AlInP cladding layers is relatively small (100 meV - 150 meV).

As the junction temperature increases, the thermal energy (k_BT) of the electrons approaches the height of this energy barrier. This allows a large fraction of the injected electrons to escape from the active quantum wells via thermionic emission into the p-type cladding region, where they recombine non-radiatively as leakage current.

4.3 Characterization of Phosphor-Converted White LEDs: Phosphor-converted white LEDs (pc-WLEDs) generate white light by combining a blue InGaN semiconductor die with an integrated yellow-emitting $Y_3A1_5O_{12}:Ce^{3+}$ (YAG:Ce) phosphor overlay. Because this design blends light from two distinct materials, its emission characteristics under varying thermal loads are more complex.

4.3.1 Asymmetric Double-Gaussian Component Modeling: The composite emission spectrum of the pc-WLED features a distinct two-peak profile: a narrow blue peak at 450 nm generated by the underlying chip and a broad yellow-green peak centered at 560 nm produced by the phosphor down-conversion layer. To analyze how temperature affects each light source independently, the collected spectra were deconvolved using an asymmetric double-Gaussian mathematical model:

$$S_{total}(\lambda) = A_1 \exp\left\{\frac{-(\lambda - \lambda_{p1})^2}{2\sigma_1^2}\right\} + A_2 \exp\left\{\frac{-(\lambda - \lambda_{p2})^2}{2\sigma_{2,asym}^2}\right\}$$

Where index 1 represents the blue semiconductor pump parameters and index 2 represents the broad yellow phosphor emission channel.

When the system is heated from 283 K to 363 K, deconvolution reveals that the two components degrade at different rates:

1. **The Blue Primary Peak (450 nm):** Follows the standard InGaN parameters described in Section 4.1, exhibiting a modest red shift (+3.5 nm) and retaining 84.5% of its optical power.
2. **The Yellow Phosphor Peak (560 nm):** Shows no significant wavelength shift, but its conversion intensity drops quickly, retaining only 73.2% of its initial output at 363 K.

This rapid loss of phosphor efficiency is caused by thermal quenching within the Ce^{3+} activator ions. Increasing the temperature enhances non-radiative relaxation from the 5d excited state back to the 4f ground state via multi-phonon emission, reducing the phosphor's overall quantum efficiency.

4.3.2 CIE 1931 Chromaticity Coordinates and Gamut Drift: Because the yellow phosphor emission decreases faster than the blue pump emission, the overall balance of light shifts with temperature. The ratio of blue to yellow photons increases, causing the overall color coordinates to slide on the CIE 1931 chromaticity diagram.

At 283 K, the chromaticity coordinates are stable at x = 0.345 and y = 0.355, located in the neutral-white region. Heating the device to 363 K shifts the coordinates to x = 0.331 and y = 0.339. This movement tracks directly toward the blue corner of the chromaticity space, narrowing the display's usable color gamut boundaries.

4.3.3 Correlated Color Temperature (CCT) and Color Rendering Index (CRI) Stability: This uneven thermal degradation causes a significant shift in the Correlated Color Temperature (CCT). Over the tested temperature range (283 K to 363 K), the calculated CCT rises from a warm-neutral white of **5020 K** to a cool, bluish-white of **5890 K**.

This represents a total upward shift of +870 K, which is easily visible to the human eye and unacceptable for architectural or commercial lighting applications requiring strict color stability.

Concurrently, the Color Rendering Index (Ra) degrades from 84.3 to 77.8. This drop is primarily driven by the narrowing and shifting of the blue peak combined with the flattening of the yellow-green phosphor spectrum. This flattening reduces the light's spectral coverage across critical red reference channels (R9), lowering the overall color rendering performance of the device at elevated temperatures.

4.4 Comprehensive Parametric Matrix Summary: To summarize the experimental results, the table below compiles the quantified electro-optical performance variations observed across all three LED categories over the 283 K to 363 K testing range.

Parameter Evaluated	**InGaN Blue LED**	**AlGaInP Red LED**	**pc-White LED (Composite)**
Initial Peak Wavelength (λ_p at **283 K**)	451.2 nm	621.5 nm	450.8 nm- 558.4 nm
Final Peak Wavelength (λ_p at **363 K**)	454.8 nm	634.1 nm	454.3 nm - 558.6 nm
Net Wavelength Shift ($\Delta\lambda_p$)	+3.6 nm	+12.6 nm	+3.5 nm - +0.2 nm
Temperature Coefficient ($d\lambda_p/dT$)	+0.045 nm/K	+0.157 nm/K	Variable Components
Initial Line width ($\Delta\lambda_{FWHM}$ at **283 K**)	18.4 nm	14.2 nm	N/A (Multi-Peak Profile)
Final Line width ($\Delta\lambda_{FWHM}$ at **363 K**)	23.1 nm	20.8 nm	N/A (Multi-Peak Profile)
Optical Power Retention (at **363 K**)	**84.2%**	**\%**	**76.8\%**
Correlated Color Temperature (CCT)	N/A	N/A	2700 K - 6500 K
Color Rendering Index (**Ra**)	N/A	N/A	84.3- 77.8

Table 2: Diverse Thermal Behaviors across Different Semiconductor Material

These findings illustrate the diverse thermal behaviors across different semiconductor material systems. The quantified coefficients and efficiency curves highlight the critical role of material selection and provide the empirical foundation needed to design effective thermal management and optical compensation strategies in high-performance applications.

V: ENGINEERING APPLICATIONS AND THERMAL MANAGEMENT

The systematic spectral shifts, linewidth broadening, and thermal efficiency losses characterized in Part 4 pose significant challenges for real-world engineering applications. In high-performance optoelectronic systems—such as automotive LED headlamps, liquid-crystal display (LCD) backlighting units, solid-state architectural illumination, and optical data links—spectral and radiometric stability is a primary design metric.

This Part bridges the gap between laboratory results and optomechanical engineering, detailing the structural, electrical, and optical strategies used to mitigate thermal degradation in modern light-emitting diode architectures.

5.1 Passive Thermal Management Architectures: Passive cooling relies on optimizing the solid-state heat conduction path to minimize the total thermal resistance ($\sigma R\theta$) between the active p-n junction (T_j) and the surrounding ambient environment (T_a). This path is governed by Fourier's Law of Heat Conduction:

$Q = -K A \nabla T$

where Q is the heat transfer rate, K is the material's thermal conductivity, A is the cross-sectional area, and ∇ T is the local temperature gradient.

5.1.1 Advanced Substrate Materials and Die Attach Technologies: The first bottleneck in passive heat dissipation occurs at the chip attachment interface. Traditional epoxy adhesives exhibit very poor thermal conductivity ($k \approx 0.2 - 0.5$ W/m. K), creating a large localized thermal barrier. Modern high-power configurations replace these polymers with advanced eutectic die attach alloys (such as $Au_{80}Sn_{20}$, $k \approx 57$ W/m. K) or nano-silver sintered pastes ($k > 150$ W/m. K).

Concurrently, the internal submount material dictates the rate of lateral heat spreading. Standard flame-retardant fiberglass substrates (FR-4) are inadequate for high-density LED arrays. High-brightness systems utilize specialized ceramic submounts with exceptional thermal capabilities:

Aluminum Oxide (**Al_2O_3**): Provides a baseline thermal conductivity of $k \approx 25 - 35$ W/m. K.

Aluminum Nitride (**AlN**): Offers an excellent thermal conductivity of $k \approx 170 - 200$ W/m. K combined with a coefficient of thermal expansion (CTE) that closely matches the GaN epitaxial layer (~4.5 \times 10^{-6} /K), minimizing thermal mechanical fatigue during rapid power cycling.

5.1.2 Metal-Core Printed Circuit Boards (MCPCBs) and Vapor Chambers: To transition heat from the individual LED package to the external environment, the submount is reflow-soldered onto a Metal-Core Printed Circuit Board (MCPCB). Unlike standard PCBs, an MCPCB features an integrated structural metal base layer:

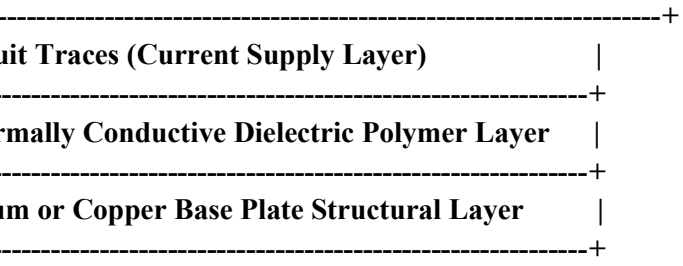

Figure 11: Layered Architecture of an MCPCB Surface

The critical engineering metric in an MCPCB is the thickness and composition of the dielectric insulation layer. Because polymers are inherently poor conductors, this layer is kept ultra-thin (30 μm - 100 μm) and is heavily doped with ceramic nanoparticles (such as AlN or BN) to achieve an effective thermal conductivity of $k \approx 3 - 8$ W/m. K.

For ultra-high power applications, such as architectural spotlighting, the MCPCB can be replaced by an integrated Vapor Chamber. This planar two-phase cooling system contains a vacuum-sealed copper envelope lined with a porous wick structure and filled with a small amount of working fluid (typically deionized water).

When heat from the LED array strikes the evaporator zone, the fluid vaporizes, absorbing its latent heat of vaporization. The vapor expands across the chamber to the cooler condenser zone, releases its heat to an external heat sink, and returns to liquid form. This phase-change cycle yields an effective thermal conductivity exceeding $k > 5000$ W/m. K, flattening localized hot spots.

5.2 Active and Dynamic Thermal Control Systems: When passive conduction pathways cannot maintain the junction temperature within optimal spectral bounds under high ambient thermal loads, active or dynamic control strategies must be deployed.

5.2.1 Forced Convection and Solid-State Peltier Regulatio: Active systems use external electrical power to accelerate heat rejection. The most common configuration combines high-surface-area pin-fin aluminum heat sinks with low-profile, pulse-width modulated (PWM) brushless DC fans. By adjusting the fan's RPM based on real-time feedback from an embedded thermistor, the system can regulate the convective heat transfer coefficient (h), stabilizing the device temperature.

For specialized industrial applications requiring strict spectral stability—such as high-resolution medical color matching or laser-diode pump sources—active Thermoelectric Coolers (TECs) are integrated directly into the LED module housing. By operating the TEC in a closed-loop configuration with an automated digital PID controller, the system can maintain the LED submount at a target temperature regardless of external weather or ambient conditions, preventing color gamut drift.

5.2.2 Active Thermal Rollback and Driver Compensation Circuits: To prevent catastrophic catastrophic optical failure or rapid aging at extreme temperatures, modern LED drivers incorporate an smart feature known as Active Thermal Rollback. The driver monitor's system temperature via an NTC thermistor network. If the temperature exceeds a pre-programmed threshold (e.g., $T_{threshold} > 353$ K), the driver's internal microprocessor dynamically limits the forward driving current (I_F), as shown below:

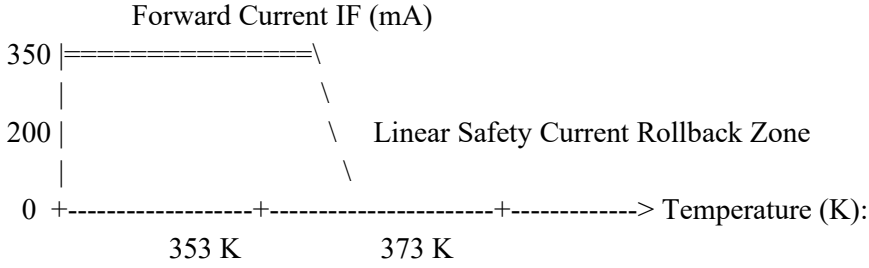

Figure 12: Active Thermal Rollback Control Curve

By rolling back the current, the driver reduces the total electrical input power ($P_{elec} = I_f.V_F$). This drops the internal heat flux (Q_{th}), preventing thermal runaway and keeping the junction temperature safely below its maximum rating ($T_{j,max} \approx 398$ K), albeit at the cost of a temporary reduction in lumen output.

5.3 Optical Stabilization and Spectral Compensation Engineering: Beyond cooling the device, engineers can use optical configuration strategies to manage the spectral shifts described in Part 4.

5.3.1 Active Closed-Loop Multi-Channel Color Tuning: Because red AlGaInP LEDs exhibit a high temperature shift coefficient (+0.157 nm/K) and severe thermal quenching compared to blue InGaN devices (+0.045 nm/K), multi-color RGBA (Red-Green-Blue-Amber) luminaire modules experience severe color rendering index (CRI) and color coordinate distortions when heated.

To maintain a stable white color point, high-end architectural fixtures use an active optical feedback network. The luminaire features an integrated multi-channel photodiode color sensor placed inside the mixing chamber to monitor the output light in real time.

If the sensor detects a drop in red intensity or a shift in color coordinates due to thermal quenching, the system's central microcontroller calculates the correction vector and independently adjusts the output currents of the individual color channels:

The drive current to the red channel is increased to compensate for the thermal efficiency drop.

The blue and green channel currents are trimmed downward to maintain a perfectly stable, constant target Correlated Color Temperature (CCT) and prevent color point drift.

5.3.2 Phosphor Material Engineering for pc-WLEDs: To improve the thermal stability of phosphor-converted white LEDs, researchers focus on enhancing the material composition of the down-conversion layer. Standard YAG:Ce^{3+} phosphors suffer from thermal quenching because their broad emission profiles are sensitive to structural lattice expansion.

Modern high-temperature white LEDs utilize advanced nitride-based phosphors doped with Europium ions, such as:

- Red-emitting Strontium Silicon Nitride ($\mathbf{Sr_2Si_5N_8:Eu^{2+}}$)
- Green-emitting Barium Silicon Oxynitride ($\mathbf{Ba_3Si_6O_{12}N_2:Eu^{2+}}$)
- The strong, highly covalent silicon-nitrogen (Si-N) network within these nitride structures provides a rigid lattice matrix with high mechanical stability and high Debye temperatures.
- This rigid structure reduces electron-phonon interactions and suppresses non-radiative relaxation pathways.

As a result, these advanced phosphors shift the thermal quenching threshold to well above 423 K (150°C), minimizing color gamut drift and ensuring consistent color quality across demanding operational environments.

5.4 Unified Multi-Domain Management Matrix: To provide a comprehensive overview of the design methodologies discussed in this chapter, the table below summarizes the thermal management options available to system engineers, categorized by operational domain.

Management Domain	**Specific Engineering Technology**	**Primary Operational Mechanism**	**Typical Performance Impact**
Material/Substrate	Aluminum Nitride (AlN) Submounts	High-conduction solid-state heat spreading	Lowers package thermal resistance to $R_\theta < 2$ K/W
Interface Optimization	Nano-Silver Sintered Die Attach	Eliminates microscopic air gaps at the chip boundary	Increases interface conductivity to k > 150 W/m. K
Structural/Passive	Vapor Chamber Systems	Multi-phase fluid evaporation and condensation cycle	Eliminates localized hot spots; effective k > 5000 W/m. K
Active Mechanical	PWM Brushless DC Cooling Fans	Forced convection boundary-layer acceleration	Significantly increases heat transfer coefficient (h)
Electrical/Driver	Intelligent Thermal Rollback Loops	Automated current limiting based on thermistor feedback	Prevents thermal runaway; protects device lifespan
Optical System	Closed-Loop Color Feedback Adjustments	Multi-channel optical sensing and dynamic current rebalancing	Eliminates chromaticity drift; stabilizes target CCT
Phosphor Chemistry	Nitride-Hosted Eu^{2+} Activators	Rigid covalent atomic frameworks	Shifts thermal quenching limits to temperatures > 423 K

Table 3: Thermal Management Options Available to System Engineers

PART 6: CONCLUSION AND FUTURE SCOPE

This concluding Part summarizes the key insights gained from this comprehensive multi-domain study, which analyzed the effects of thermal loading on the physics, performance, and operational lifespan of light-emitting diodes (LEDs). By matching advanced solid-state theory with high-resolution spectroradiometric measurements, this investigation quantified how temperature fundamentally alters the emission profiles of direct-bandgap semiconductor devices.

Building on these findings, we highlight the main contributions of this work and outline future research directions aimed at developing the next generation of smart, thermally resilient solid-state illumination systems.

6.1 Comprehensive Summary of Research Contributions: This work systematically examined the interactions between thermal energy, quantum mechanical configurations, and material structures across three core LED architectures: monochromatic InGaN blue, monochromatic AlGaInP red, and phosphor-converted white LEDs (pc-WLEDs). The key analytical and empirical findings are summarized below:

1. **Material-Specific Bandgap Sensitivity:** The experiment confirmed a clear difference in thermal stability between different semiconductor alloy systems. The quaternary AlGaInP red LED exhibited a steep temperature coefficient ($d\lambda_p/dT \approx +0.157$ nm/K), making it three times more sensitive to thermal shifts than the ternary InGaN blue LED ($d\lambda_p/dT \approx +0.045$ nm/K). This difference stems directly from the lower Debye temperature and weaker interatomic bonding energies inherent to the phosphide crystal lattice.
2. **Validation of Linewidth Broadening Models:** High-resolution spectral tracking validated the theoretical Maxwell-Boltzmann carrier distribution model, which predicts a linear broadening of the emission linewidth proportional to 1.8 k_BT. In GaN devices, this thermal broadening is superimposed on a significant, temperature-independent inhomogeneous broadening component (~45 meV) caused by nanoscale fluctuations in local Indium composition and quantum well thickness.
3. **Deconvolution of Thermal Quenching Pathways:** Using an asymmetric double-Gaussian model to deconvolve the emission spectra of pc-WLEDs revealed that the system's color instability is driven by two competing decay mechanisms. While the blue pump die loses efficiency due to non-radiative Shockley-Read-Hall (SRH) defect recombination, the yellow YAG:Ce phosphor degrades independently through thermal quenching of its Ce^{3+} activator ions. This uneven degradation shifts the overall color coordinates toward the blue spectrum, causing the Correlated Color Temperature (CCT) to rise by +870 K over an 80 K temperature span.
4. **Validation of Non-Invasive Junction Sensing:** The study successfully validated a dual junction-temperature tracking protocol. By matching the electrical Forward Voltage (V_F) temperature-coefficient method with a JEDEC-standard steady-state thermal resistance network model, the system monitored the internal temperature of the active p-n junction in real time with an accuracy of \pm 0.4 K.

6.2 Future Horizons and Research Opportunities: While this study established a rigorous baseline for understanding and mitigating thermal effects in conventional LED systems, emerging applications continue to push the boundaries of solid-state efficiency, color purity, and power density. Several promising research avenues have been identified to guide future investigations:

6.2.1 Thermal Modeling of Ultrafast Micro-LED (uLED) Arrays: The rapid development of augmented reality (AR) micro-displays, wearable smart devices, and high-speed visible light communication (VLC or Li-Fi) systems has driven the need for ultra-small pixel configurations known as Micro-LEDs (uLEDs), where individual pixel diameters drop below 10 μm.

At these microscopic scales, standard bulk thermal models break down. Micro-LED arrays exhibit an extremely high surface-perimeter-to-area ratio, which accelerates non-radiative surface recombination along the etched sidewalls of the pixels. This concentrated recombination generates high localized heat densities that can severely degrade optical performance.

Future research should focus on developing multi-scale, transient hydrodynamic heat transfer models. These models must incorporate localized surface carrier dynamics to optimize sidewall passivation techniques and maximize efficiency in high-density micro-displays.

6.2.2 Quantum Dot Color-Conversion (QDCC) Optimization: Rather than relying on conventional rare-earth powder phosphors, next-generation display architectures are shifting toward Quantum Dot Color-Conversion (QDCC) layers. These layers use colloidal semiconductor nanocrystals—such as Cadmium Selenide (CdSe) or Lead Halide Perovskites ($CsPb_X3$)—to convert blue pump light into highly saturated, narrow-band red and green emission profiles.

However, quantum dots are highly susceptible to thermal degradation. At elevated operating temperatures, the tight quantum confinement structure can trigger accelerated Auger recombination and thermal carrier escape into surface trap states. This causes severe thermal quenching and permanent optical bleaching of the nanocrystals.

Future work should investigate the synthesis of advanced "giant" core-shell heterostructures (e.g., CdSe/CdS) or the encapsulation of quantum dots inside protective, highly conductive inorganic silica matrices to shield the active cores from both thermal and environmental degradation.

6.2.3 Smart Solid-State Lighting via Per-Pixel Integrated Electronics: To completely eliminate the color drifts caused by uneven thermal quenching, future packaging designs must move beyond basic system-level thermal rollback loops. The ultimate goal is the realization of Smart Solid-State Lighting Architecture.

This approach involves monolithically integrating high-electron-mobility transistors (HEMTs) and micro-scale thin-film thermistors directly onto the same Gallium Nitride silicon wafer substrate as the light-emitting quantum wells.

By embedding smart processing electronics into every individual pixel, each light-emitting element can autonomously monitor its own internal junction temperature and adjust its local driving current in real time. This per-pixel modulation will enable self-calibrating, smart luminaires capable of maintaining perfect color rendering and constant color coordinates across their entire operational lifespan, regardless of extreme environmental fluctuations.

References

1. Vivek M, Swami K, Mittal MK. Experimental Study of Light Dependent Resistor (LDR) & Its Application in Energy Efficient Automation.
2. Bhattarai, T., Ebong, A., & Raja, M. (2024). A Review of Light-Emitting Diodes and Ultraviolet Light-Emitting Diodes and Their Applications. Photonics, 11(6), 491.
3. Höpfner, J., Gupta, P., Guttmann, M., Ruschel, J., Glaab, J., Kolbe, T., Rass, J., Knauer, A., Stölmacker, C., Einfeldt, S., Wernicke, T., Weyers, M., & Kneissl, M. (2023).
4. Temperature-dependent electroluminescence of stressed and unstressed InAlGaN multi-quantum well UVB LEDs. Applied Physics Letters, 122(15), 151104.
5. Jeong, S. S., & Ko, J.-H. (2012). Analysis of the spectral characteristics of white light-emitting diodes under various thermal environments. Journal of Information Display, 13(1), 37–42.
6. Kwak, K., Cho, K., & Kim, S. (2013). Analysis of thermal degradation of organic light-emitting diodes with infrared imaging and impedance spectroscopy. Optics Express, 21(24), 29558.
7. Liu, Z., Li, P., Jiang, H., & Wang, D. (2021). Application of color temperature controllability in LED lighting environment of highway tunnel. E3S Web of Conferences, 233, 01101.
8. Titkov, I., Karpov, S., Yadav, A., Mamedov, D., Zerova, V., & Rafailov, E. (2017). Efficiency of True-Green Light Emitting Diodes: Non-Uniformity and Temperature Effects. Materials, 10(11), 1323.